



OPEN

Thermal growth in solar water pump using Prandtl–Eyring hybrid nanofluid: a solar energy application

Wasim Jamshed¹✉, Nor Ain Azeany Mohd Nasir², Siti Suzilliana Putri Mohamed Isa³, Rabia Safdar^{4,5}, Faisal Shahzad¹, Kottakaran Soopy Nisar⁶, Mohamed R. Eid^{7,8}, Abdel-Haleem Abdel-Aty^{9,10} & I. S. Yahia^{11,12,13}

Nowadays, with the advantages of nanotechnology and solar radiation, the research of Solar Water Pump (SWP) production has become a trend. In this article, Prandtl–Eyring hybrid nanofluid (P-EHNF) is chosen as a working fluid in the SWP model for the production of SWP in a parabolic trough surface collector (PTSC) is investigated for the case of numerous viscous dissipation, heat radiations, heat source, and the entropy generation analysis. By using a well-established numerical scheme the group of equations in terms of energy and momentum have been handled that is called the Keller-box method. The velocity, temperature, and shear stress are briefly explained and displayed in tables and figures. Nusselt number and surface drag coefficient are also being taken into reflection for illustrating the numerical results. The first finding is the improvement in SWP production is generated by amplification in thermal radiation and thermal conductivity variables. A single nanofluid and hybrid nanofluid is very crucial to provide us the efficient heat energy sources. Further, the thermal efficiency of MoS₂-Cu/EO than Cu-EO is between 3.3 and 4.4%. The second finding is the addition of entropy is due to the increasing level of radiative flow, nanoparticles size, and Prandtl–Eyring variable.

Green electric energy is attained from the heat radiated and converted light from the sun. Aside from the fact that solar energy is renewable, it requires minimal maintenance and it can also generate electricity and heat, which may cause a depletion in power costs. We have two primary forms of solar energy: photovoltaic (PV) and concentrated solar power (CSP). In the PV solar panels, sun rays are stored by solar cells, which are then transformed directly into energy. The primary application of PV systems, combined with the solar battery, are (i) public lighting (billboards, highway, parking lots)¹, (ii) amplification of signals in communication systems (wireless)², and (iii) solar water pump³.

Meanwhile, CSP systems use mirrors (lenses and reflectors) to collect sun rays to heat a liquid substance. The high temperature of the liquid in CSP causes a heat engine to work. The main applications of CSP are (i) water heating for hostel⁴, (ii) greenhouse plants⁵, and (iii) biogas production⁶. Furthermore, CSP systems are effective in storing energy using thermal energy storage technologies (TES). Therefore, CSP systems can be employed

¹Department of Mathematics, Capital University of Science and Technology (CUST), Islamabad 44000, Pakistan. ²Department of Mathematics, Centre for Defence Foundation Studies, Universiti Pertahanan Nasional Malaysia, Kem Sungai Besi, 57000 Kuala Lumpur, Malaysia. ³Institute for Mathematical Research, Universiti Putra Malaysia, 43400 UPM Serdang, Selangor Darul Ehsan, Malaysia. ⁴Department of Mathematics, University of Jhang, Jhang 35200, Pakistan. ⁵Department of Mathematics, Lahore College for Women University, Lahore 54000, Pakistan. ⁶Department of Mathematics, College of Arts and Sciences, Prince Sattam Bin Abdulaziz University, Wadi Aldawaser 11991, Saudi Arabia. ⁷Department of Mathematics, Faculty of Science, New Valley University, Al-Kharga, Al-Wadi Al-Gadid 72511, Egypt. ⁸Department of Mathematics, Faculty of Science, Northern Border University, Arar 1321, Saudi Arabia. ⁹Department of Physics, College of Sciences, University of Bisha, P.O. Box 344, Bisha 61922, Saudi Arabia. ¹⁰Physics Department, Faculty of Science, Al-Azhar University, Assiut 71524, Egypt. ¹¹Advanced Functional Materials and Optoelectronic Laboratory (AFMOL), Department of Physics, Faculty of Science, King Khalid University, P.O. Box 9004, Abha, Saudi Arabia. ¹²Research Center for Advanced Materials Science (RCAMS), King Khalid University, P.O. Box 9004, Abha 61413, Saudi Arabia. ¹³Nanoscience Laboratory for Environmental and Biomedical Applications (NLEBA), Semiconductor Lab., Department of Physics, Faculty of Education, Ain Shams University, Roxy, Cairo 11757, Egypt. ✉email: wasiktk@hotmail.com

for no or low sunlight, e.g., on the weathers of clouds or in the nighttime, to produce electric power. This methodology enhances the usage of the technology of solar thermal conductivity as it can deal with environmental limitations. CSP systems are the most fascinating due to high power generation because they utilized TES. This type of thermal storage (TES) is considered more efficient in a solar battery because it can control energy supply and demand. Besides, the utilization of TES reduces the following factors: energy demand, energy consumption, and cost. In a conclusion, the efficiency of CSP systems can be enhanced⁷. Advantages of combining storage and solar battery are balancing electricity loads, stability solar generation, and providing resilience.

Solar Water Pumps (SWP) is one of the applications from PV solar systems, which produces electricity to pump water. Typical applications are water for the agricultural sector⁸, crop irrigation⁹, and livestock¹⁰. In 1901, A. Eneas built the giant solar water pump globally at the Ostrich Farm in Pasadena, California, USA¹¹. Subsequently, in 1920, Harrington from New Mexico was the first one who used the solar concentrating technology [also known as concentrated solar power (CSP)], in the form of the solar-powered steam engine to pump water up to a height of 6 m¹¹. In conclusion, the literature review proved that SWP applied both solar technology: PV and CSP, to perform its works.

One type of CSP is parabolic trough solar collector (PTSC), which has four fundamental elements: collector, receiver, heat transfer fluid (HTF), and heat engine. A collector is a reflecting surface that uses a parabolic mirror to reflect the collective thermal energy from the sun to the receiver. This receiver transfers the heat to the focal line, which is filled with an HTF. The temperature of HTF will become very high (almost 390 °C), and it will flow to the heat engine to generate electricity. The heat transfer in HTF is a cyclic process, where the process is continued in the power generation systems. The ideal characteristics of HTF in PTSC are: can work at high temperature, stable at high temperature, minimum viscosity, minimum vapor pressure, the minimum point of freezing, low maintenance including costs, non-corrosive, and proven as safe¹². Lately, it is found that nanofluids are particular HTF with advanced thermal and optical characteristics. The most usual nanoparticles in a nanofluid as HTF in PTSC are metallic and non-metallic nanoparticles. Some of the examples of metallic nanoparticles in nanofluid as HTC are Al¹³, Au¹⁴, Ag, and Cu¹⁵. Meanwhile, non-metallic nanoparticles consisting of the examples of ZnO¹⁴, CeO₂¹⁶, NiFe₂O₄¹⁷, Fe₂O₃¹⁸, Fe₃O₄¹⁹, SiO₂, CuO, TiO₂, and Al₂O₃²⁰. Other types of particles in nanofluid, such as carbon nanotubes (CNT)²¹, single-walled carbon nanotubes (SWCNT)²², and multi-walled carbon nanotubes (MWCNT)²³ also being applied in the experimental and numerical works in PTSC.

Hybrid nanofluid has become one of the selections as HTF in PTSC due to its higher thermal conductivity²⁴ than nanofluid. It is prepared by dispersing two or more different nanoparticles in the base fluid. Studies using hybrid nanofluids in PTSC have been reported, by considering the following nanoparticles: Ag–MgO/water¹³, GO–Co₃O₄/60EG:40 W¹³, Cu–Al₂O₃/water¹³, Al₂O₃–TiO₂/Syltherm 800²⁵, Ag–ZnO/Syltherm 800, Ag–TiO₂/Syltherm 800, and Ag–MgO/Syltherm 800²⁶.

The entropy of an isolated system is continuously increasing that is the second law of thermodynamics. Therefore, some studies have described this law in thermal system performance²⁷ and heat transfer in nanofluid²⁸. Moreover, entropy generation causes a decline in the thermal system²⁹. So, the researchers must find a way to control the entropy level to increase the thermal conduction in flowing fluid. One of the solutions is to include entropy in their fluid flow model. The recent studies of entropy in hybrid nanofluid have been reported^{30–37}. The magnetohydrodynamics (MHD) flow of water based hybrid nanofluid was examined by Khan et al.³⁰ and Shah et al.³¹. In contrast, the MHD hybrid nanofluid where the base fluid is Ethylene glycol was described by Aziz et al.³². The effect of thermal radiation was studied by Jamshed and Aziz³³ and Aziz et al.³⁴, where ethylene glycol³³ and water³⁴ were acting as a base for hybrid nanofluid. In addition, Jamshed and Aziz³³ studied the Casson hybrid nanofluid, whereas Aziz et al.³⁴ analyzed the Powell–Eyring hybrid nanofluid. The thermal characteristics of hybrid nanofluid in the various shape of container or boundary, such as in microchannel³⁵, rotating channel³⁶, and wavy cavity³⁷, were reported. These studies were emphasizing the model of Cu–Ti and C71500 water-base fluid³⁵, Cu–Al₂O₃ ethylene glycol base fluid³⁶, and Cu–Al₂O₃ water-base fluid³⁷.

The Prandtl–Eyring fluid (PEF) is a type of non-Newtonian viscoelastic fluid ideal talented of labeling nil shear degree viscosity possessions which widening of a mass tempts the flow. The scientific preparation of the issue provides an exceedingly set of nonlinear partial differential equations. Arif et al.³⁸ establish a theoretical review to detect the impacts of a customarily employed magnetic field on PEF flow through a linearly stretchable surface. Abbas et al.³⁹ studied a three-dimensional axisymmetric inactivity flow using PEF. Khan et al.⁴⁰ proposed a mathematical analysis of bio convection on PEF, whereas Abdelmalek et al.⁴¹ investigated the influences of Brownian motion and thermo/phonetic stress on a thermal exchange of PFF produced by strained shallow. Abbasi et al.⁴² studied the effects on electro-osmosis-modulated peristaltic flow of PEF through the pointed strait. Finally, Yong et al.⁴³ and Imran et al.⁴⁴ presented a mathematical modeling system having the PEF flow. Recent additions considering nanofluids with heat and mass exchange in different physical aspects are given by^{33, 34, 45–58}.

Based on the debates above, the main objective of the present exploration focuses on the influences of viscous dissipation, heat radiations, heat source, and entropy generation analysis on Prandtl–Eyring hybrid nanofluid flow (P-EHNF) which is chosen as a working fluid in the production of SWP in PTSC is investigated. Cu and MoS₂ nanoparticles in EO as a base fluid are considered. The comparing of thermal features between the single (Cu–EO) and hybrid (MoS₂–Cu/EO) nanofluid are demonstrated. By using a well-established numerical scheme the group of equations in terms of energy and momentum have been handled that is called the Keller-box method. The velocity, temperature, and shear stress are briefly explained and displayed in tables and figures. Nusselt number and surface drag coefficient are also being taken into reflection for illustrating the numerical results. Figure 1 represents a parabolic trough solar collector in a water pump.

Novelty of current work. A mathematical formulation of solar water pumps using Prandtl–Eyring and PTSC hybrid nanofluid was originated accordingly in the earlier studies, which were explained in the previ-

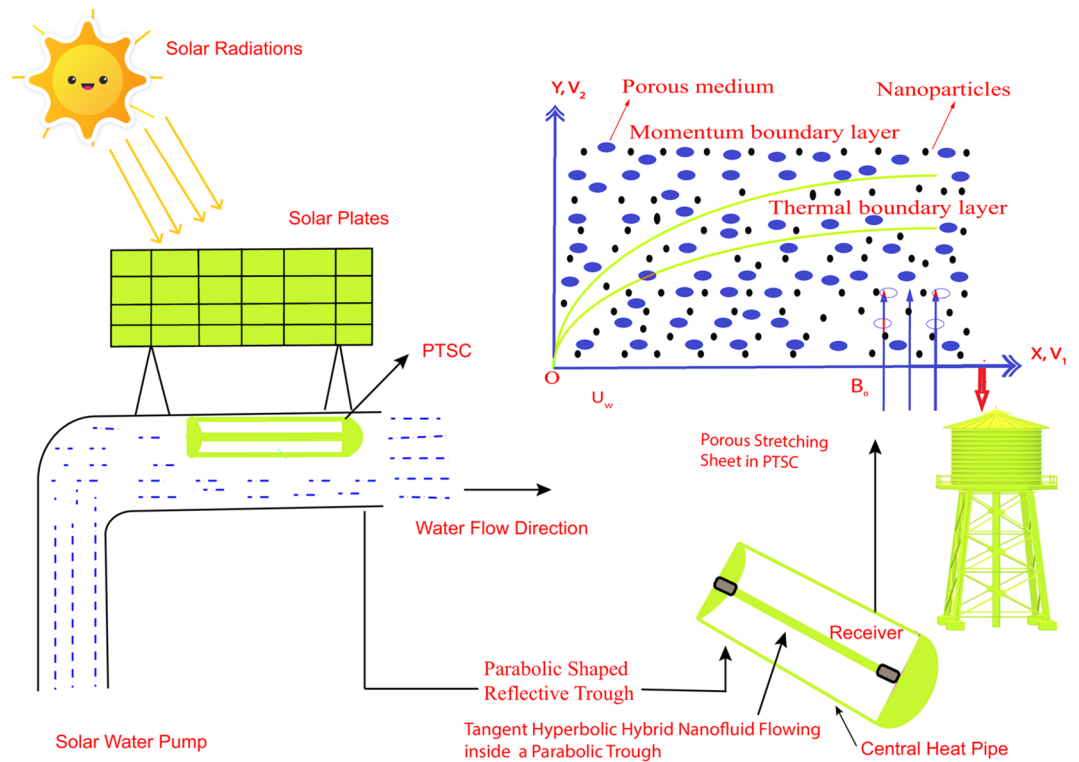


Figure 1. The theoretical experiment of a solar water pump.

ous sections. Molybdenum disulfide oxide (MoS_2) and Copper (Cu) are the types of nanoparticles in this fluid because engine oil is the base fluid (EO). This article's crucial contribution includes the following: there has been no actual achievement of this initial theoretical experiment. The third-world or undeveloped nations can use this PTSC as a radical source of energy by exploiting the light and heat from the sun. Our analysis uses PTSC, which needs the selection of a suitable working fluid. In a conclusion, hybrid nanofluid has replaced nanofluid as our first option due to the variety that it has a greater rate of heat transmission.

Outline of current work. Our paper has been structured as:

- In section “**Flow model formulations**”, we gave a regarding mathematical formulated.
- In section “**Dimensionless formulations model**”, we have developed the solution to the problem.
- The numbering process was provided in section “**Classical Keller-box technique**”, the Keller-box system.
- Then in section “**Code verification**”, we developed code validation.
- In section “**Entropy analysis**”, we analyzed the development of entropy.
- In section “**Results and discussion**”, we summarized the findings and the debate.
- Finally, in section “**Final results and future guidance**”, we have achieved the final results and futuristic guidelines.

Flow model formulations

The equations of the mathematical flow model illustrated a horizontally moving plate through an uneven expansion velocity $U_w(x, 0)$, given that b is the unique expansion rate such as:

$$U_w(x, 0) = bx. \quad (1)$$

The remote exterior temperature is denoted by $\mathbb{Y}_w(x, t) = \mathbb{Y}_\infty + b^*x$ whereas it supposedly will become constant when $x = 0$. The notation \mathbb{Y}_∞ , \mathbb{Y}_w and b^* gave out the meaning of temperature of neighboring, exterior as well as variation rate, congruently. Besides being slippery, the plate's surface is sensitive to temperature fluctuations. At an interaction volume fraction (ϕ_{Cu}), a fixed value of 0.09 Cu nano solid-particles are added to the EO-based fluid to produce a hybrid nanofluid for this study. A hybrid nanofluid composed of molybdenum disulfide (MoS_2) nano molecules have been created at a concentrated size ϕ_{Ms} .

Suppositions and terms of model. The principles and constraints apply to the flow model can be described as follows:

- 2-D laminar flowing.

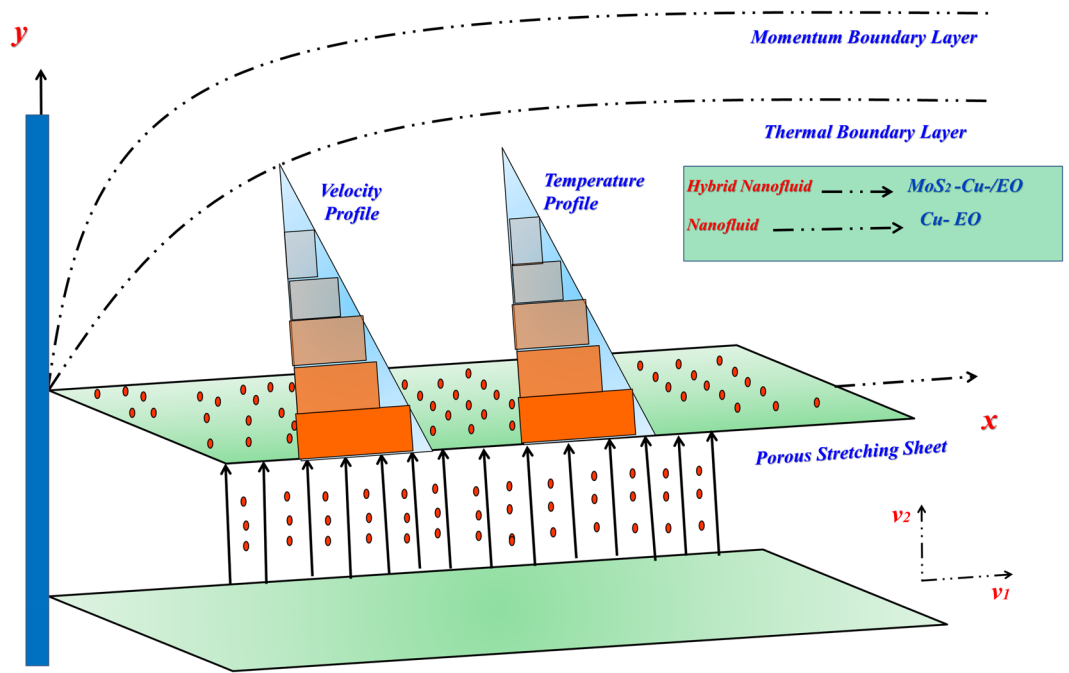


Figure 2. Diagram of the flow model.

- Boundary-layer approximations.
- Single phase (Tiwari-Das) scheme.
- Solar water pump.
- Parabolic trough solar collector.
- Non-Newtonian P-EHNF.
- Porous media.
- Thermal radiative flow.
- Nano solid-particles shape-factor.
- Porousnesselongated surface.
- Convection and slippery boundary constraints.

Geometric model. The geometric flowing model is displayed as in Fig. 2:

Model equations. The constitutive flow formulas⁴⁵ of the viscous Prandtl–Eyring hybrid nanofluid, in combination with a porous media, viscous dissipation, and thermal radiative flow utilizing the approximate boundary layer, are

$$\frac{\partial v_1}{\partial x} + \frac{\partial v_2}{\partial y} = 0, \tag{2}$$

$$v_1 \frac{\partial v_1}{\partial x} + v_2 \frac{\partial v_1}{\partial y} = \frac{A_d}{C\rho_{hnf}} \left(\frac{\partial^2 v_1}{\partial y^2} \right) - \frac{A_d}{2C^3\rho_{hnf}} \frac{\partial^2 v_1}{\partial y^2} \left[\left(\frac{\partial v_1}{\partial y} \right)^2 \right] - \frac{\mu_{hnf}}{\rho_{hnf}k} v_1, \tag{3}$$

$$v_1 \frac{\partial \Psi}{\partial x} + v_2 \frac{\partial \Psi}{\partial y} = \frac{k_{hnf}}{(\rho C_p)_{hnf}} \left(\frac{\partial^2 T}{\partial y^2} \right) - \frac{1}{(\rho C_p)_{hnf}} \left(\frac{\partial q_r}{\partial y} \right) + \frac{1}{(\rho C_p)_{hnf}} Q_L(T - T_\infty) + \frac{\mu_{hnf}}{(\rho C_p)_{hnf}} \left(\frac{\partial v_1}{\partial y} \right)^2. \tag{4}$$

The related boundary constraints are Aziz et al.⁴⁶:

$$v_1(x, 0) = U_w + N_L \left(\frac{\partial v_1}{\partial y} \right), v_2(x, 0) = V_w, \quad -k_L \left(\frac{\partial \Psi}{\partial y} \right) = h_L(\Psi_w - \Psi), \tag{5}$$

$$v_1 \rightarrow 0, \quad \Psi \rightarrow \Psi_\infty \text{ as } y \rightarrow \infty. \tag{6}$$

where the component of flowing velocity can be prescribed as $\vec{v} = [v_1(x, y, 0), v_2(x, y, 0), 0]$. We consider Ψ as the temperature of the fluid. Other vital quantities are fluid parameters A_d and C , surface permeability V_w , heat transfer coefficient h_L , porosity (k) and thermal conductivity of solid k_L . Physical behaviours comprising

Features	Nanoliquid
Dynamical viscidness (μ)	$\mu_{nf} = \mu_f(1 - \phi)^{-2.5}$
Density (ρ)	$\rho_{nf} = (1 - \phi)\rho_f + \phi\rho_s$
Heat capacity (ρC_p)	$(\rho C_p)_{nf} = (1 - \phi)(\rho C_p)_f + \phi(\rho C_p)_s$
Thermal conductivity (κ)	$\frac{\kappa_{nf}}{\kappa_f} = \left[\frac{(\kappa_s + 2\kappa_f) - 2\phi(\kappa_f - \kappa_s)}{(\kappa_s + 2\kappa_f) + \phi(\kappa_f - \kappa_s)} \right]$

Table 1. Thermo-physical features for nanoliquids. ϕ is the nano solid-particle size coefficient. $\mu_f, \rho_f, (C_p)_f$ and κ_f are dynamical viscidness, intensity, operative heat capabilities, and thermal exchange of the standard fluid respectively. The useless characteristics $\rho_s, (C_p)_s$ and κ_s are the intensity, effective heat capacitance, and thermal conductance of the nanomolecules, correspondingly

Features	Hybrid nanofluid
Viscosity (μ)	$\mu_{hnf} = \mu_f(1 - \phi_{Cu})^{-2.5}(1 - \phi_{Ms})^{-2.5}$
Density (ρ)	$\rho_{hnf} = [(1 - \phi_{Ms})\{(1 - \phi_{Cu})\rho_f + \phi_{Cu}\rho_{p1}\}] + \phi_{Ms}\rho_{p2}$
Heat capacity (ρC_p)	$(\rho C_p)_{hnf} = [(1 - \phi_{Ms})\{(1 - \phi_{Cu})(\rho C_p)_f + \phi_{Cu}(\rho C_p)_{p1}\}] + \phi_{Ms}(\rho C_p)_{p2}$
Thermal conductivity (κ)	$\frac{\kappa_{hnf}}{\kappa_f} = \left[\frac{(\kappa_{p2} + 2\kappa_{gf}) - 2\phi_{Ms}(\kappa_{gf} - \kappa_{p2})}{(\kappa_{p2} + 2\kappa_{gf}) + \phi_{Ms}(\kappa_{gf} - \kappa_{p2})} \right]; \frac{\kappa_{gf}}{\kappa_f} = \left[\frac{(\kappa_{p1} + 2\kappa_f) - 2\phi_{Cu}(\kappa_f - \kappa_{p1})}{(\kappa_{p1} + 2\kappa_f) + \phi_{Cu}(\kappa_f - \kappa_{p1})} \right]$

Table 2. Thermo-physical properties of hybrid nanofluids.

Thermophysical	ρ (kg/m ³)	c_p (J/kg K)	k (W/mK)
Copper (Cu)	8933	385	401
Engine oil (EO)	884	1910	0.144
Molybdenum disulfide (MoS ₂)	5060	397.746	34.5
(Cu-EO) P-ENF	2332.82	765,464	0.30573
(MoS ₂ -Cu/EO) P-EHNF	2823.71	2,005,201	0.63584

Table 3. Fabricated materials thermo-physical attributes.

convectonal heated surface approaches to its thermal wastage by the application of conduction (Newtonian heating), and flow velocity in the neighboring of the surface has a direct behaviour to the shear stress exerts in it (slip condition) are taken into account.

Thermo-physical properties of P-ENF. Nano solid particles dispersed in EO induce improved thermo-physical characteristics. The following Table 1 equations summarize P-ENF substance variables^{47, 48}.

Thermo-physical properties of P-EHNF. The primary assumption of hybrid nanofluids is the insertion of two distinct nanosolid particles inside the basis fluid⁴⁹. Theseacts improve the capacity for heat transmission of common liquids and are a maximum heat interpreter under nanofluids. P-EHNF variables content is summarized in Table 2^{33, 34}.

In Table 2, $\mu_{hnf}, \rho_{hnf}, \rho(C_p)_{hnf}$ and κ_{hnf} are hybrid nanofluid dynamical viscidness, intensity, consistent heat capability, and thermal conduction. ϕ is the volume of solid nanomolecules coefficient for mono nanofluid and $\phi_{hnf} = \phi_{Cu} + \phi_{Ms}$ is the nano soli-particles size coefficient for the mixture of nanofluid. $\mu_f, \rho_f, (C_p)_f, \kappa_f$ and σ_f are dynamical viscidness, density, specific heat capacitance, and thermal conduction of the basefluid. $\rho_{p1}, \rho_{p2}, (C_p)_{p1}, (C_p)_{p2}, \kappa_{p1}$ and κ_{p2} are the intensity, specific heat capacitance, and thermal conductance of the nanomolecules.

Nano solid-particles and basefluid lineaments. In this analysis, the material characteristics of the primary engine oil-based liquid of the engine are specified in Table 3^{50, 51}.

Rosseland approximation. Radiative flow only passes a shortened distance because its non-Newtonian P-EHNF is thicker. Because of this, the approximation for radiative fluxing from Rosseland⁵² is utilized in the formula (4).

$$q_r = -\frac{4\sigma^*}{3k^*} \frac{\partial T^4}{\partial y}, \tag{7}$$

herein, σ^* signifies the constant worth of Stefan-Boltzmann and k^* symbols the rate.

Dimensionless formulations model

In the study of the similarity technology that transmutes the governing PDEs into ODEs, the BVP formulas (2)–(6) are modified. Familiarizing stream function ψ in the formula

$$v_1 = \frac{\partial \psi}{\partial y}, v_2 = -\frac{\partial \psi}{\partial x}. \tag{8}$$

The specified similarity quantities are

$$\Gamma(x, y) = \sqrt{\frac{b}{v_f}}y, \quad \psi(x, y) = \sqrt{v_f b x} f(\chi), \quad \theta(\chi) = \frac{\Upsilon - \Upsilon_\infty}{\Upsilon_w - \Upsilon_\infty}. \tag{9}$$

into Eqs. (2)–(6). We get

$$\alpha^* f'''(1 - \beta^* f'^2) + \phi_b [ff'' - f'^2] - \frac{1}{\phi_a} K f' = 0, \tag{10}$$

$$\theta'' \left(1 + \frac{1}{\phi_d} P_r N_L \right) + P_r \frac{\phi_c}{\phi_d} \left[f\theta' - f'\theta + \frac{E_L}{\phi_a \phi_c} f'^2 \right] = 0. \tag{11}$$

with

$$\left. \begin{aligned} f(0) = S, f'(0) = 1 + \Lambda_L f''(0), \quad \theta'(0) = -G_L(1 - \theta(0)) \\ f'(\Gamma) \rightarrow 0, \theta(\Gamma) \rightarrow 0, as \Gamma \rightarrow \infty \end{aligned} \right\} \tag{12}$$

where ϕ'_i is $a \leq i \leq d$ in formulas (10) and (11) signify the subsequent thermo-physical structures for P-HNF

$$\phi_a = (1 - \phi_{Cu})^{2.5} (1 - \phi_{Ms})^{2.5}, \phi_b = (1 - \phi_{Ms}) \left[(1 - \phi_{Cu}) + \phi_{Cu} \frac{\rho_{p1}}{\rho_f} \right] + \phi_{Ms} \frac{\rho_{p2}}{\rho_f}, \tag{13}$$

$$\phi_c = (1 - \phi_{Ms}) \left\{ (1 - \phi_{Cu}) + \phi_{Cu} \frac{(\rho C_p)_{p1}}{(\rho C_p)_f} \right\} + \phi_{Ms} \frac{(\rho C_p)_{p2}}{(\rho C_p)_f}, \tag{14}$$

$$\phi_d = \left[\frac{(\kappa_{p2} + 2\kappa_{nf}) - 2\phi_{Ms}(\kappa_{nf} - \kappa_{p2})}{(\kappa_{p2} + 2\kappa_{nf}) + \phi_{Ms}(\kappa_{nf} - \kappa_{p2})} \right] \left[\frac{(\kappa_{p1} + 2\kappa_f) + \phi_{Cu}(\kappa_f - \kappa_{p1})}{(\kappa_{p1} + 2\kappa_f) - 2\phi_{Cu}(\kappa_f - \kappa_{p1})} \right]. \tag{15}$$

Description of the embedded control physical parameters. Equation (2) is precisely approved. In already discussed equations, the notation ' was employed for expressing the derivatives related to Γ . Here

Parameter	Name	Expression	Default value
α^*	Prandtl–Eyring parameter-I	$\alpha^* = \frac{A_d}{\mu R C}$	1.0
β^*	Prandtl–Eyring parameter-II	$\beta^* = \frac{b^* x^2}{2C^2 v_f}$	0.4
P_r	Prandtl number	$P_r = \frac{\nu_f}{\alpha_f}$	6450
ϕ	Volume fraction	ϕ	0.18
K	Porosity parameter	$K = \frac{\nu_f}{bk}$	0.1
S	Suction/injection parameter	$S = -V_w \sqrt{\frac{1}{v_f b}}$	0.4
N_r	Thermal radiation parameter	$N_L = \frac{16}{3} \frac{\sigma^* T_\infty^3}{\kappa^* \nu_f (\rho C_p)_f}$	0.3
G_L	Biot number	$G_L = \frac{h_L}{L} \sqrt{\frac{\nu_f}{b}}$	0.3
E_L	Eckert number	$E_L = \frac{U_w^2}{(C_p)_f (\Upsilon_w - \Upsilon_\infty)}$	0.3
Λ_L	Velocity slip	$\Lambda_L = \sqrt{\frac{b}{v_f}} \mu_f$	0.3

Drag force and Nusselt number. The drag force (C_f) combined with the Nusselt amount (Nu_x) are the interesting physical amounts that controlled the flowing and specified as⁴⁵

$$C_f = \frac{\tau_w}{\frac{1}{2} \rho_f U_w^2}, \quad Nu_x = \frac{x q_w}{k_f (\Upsilon_w - \Upsilon_\infty)} \tag{16}$$

where τ_w and q_w determine as

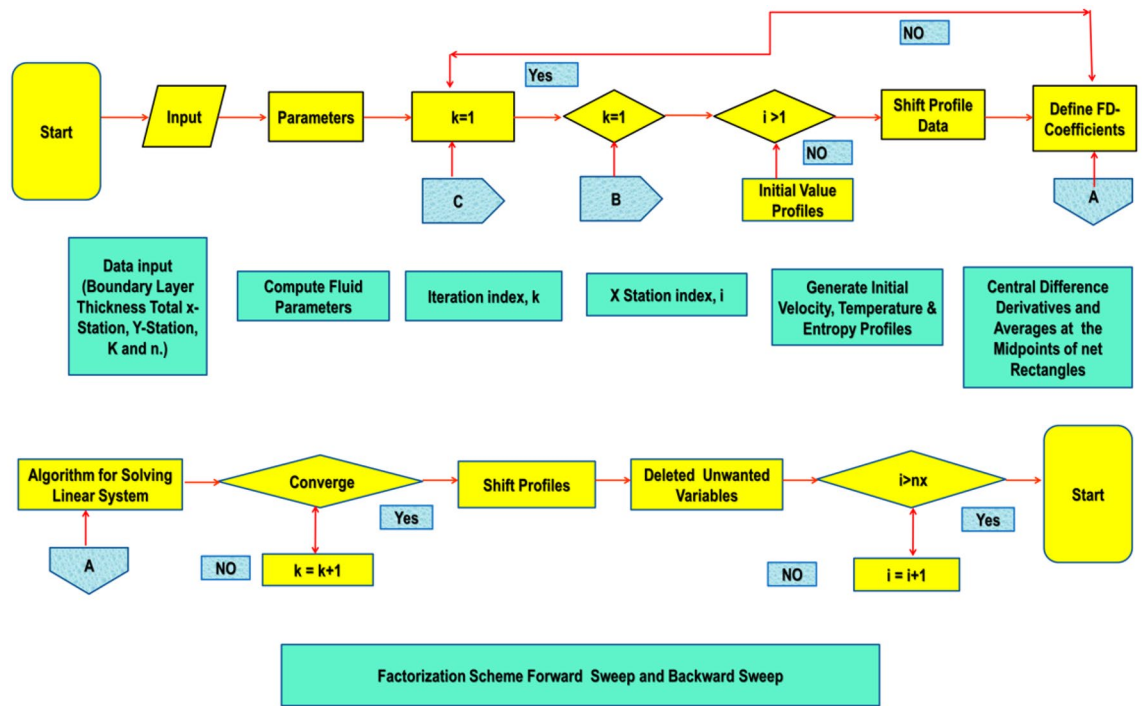


Figure 3. Chart of KBM steps.

$$\tau_w = \left(\frac{A_d}{C} \frac{\partial v_1}{\partial y} + \frac{A_d}{6C^3} \left(\frac{\partial v_1}{\partial y} \right)^3 \right)_{y=0}, q_w = -k_{hmf} \left(1 + \frac{16}{3} \frac{\sigma^* \Xi_\infty^3}{\kappa^* \nu_f (\rho C_p)_f} \right) \left(\frac{\partial \Xi}{\partial y} \right)_{y=0} \quad (17)$$

The dimensionless transmutations (9) are implemented to obtain

$$C_f Re_x^{\frac{1}{2}} = \alpha^* f''(0) - \frac{1}{3} \alpha^* \beta^* (f''(0))^3, \quad Nu_x Re_x^{-\frac{1}{2}} = -\frac{k_{hmf}}{k_f} (1 + N_L) \chi'(0), \quad (18)$$

where Nu_x increases the amount of Nusselt and C_f causes an increment in the drag force coefficient. $Re_x = \frac{u_w x}{\nu_f}$ is local Re based on the elongated velocity $u_w(x)$.

Classical Keller-box technique

Because of its rapid convergence, the Keller-box approach (KBM)⁵³ is used to find solutions for model formulas (Fig. 3). KBM is used to find the localized solve of (10) and (11) with constraints (12). The policy of KBM is specified as next.

Stage 1: ODEs adaptation. In the early stage, all of the ODEs must be transformed into 1st-order ODEs (10)–(12)

$$z_1 = f', \quad (19)$$

$$z_2 = z_1', \quad (20)$$

$$z_3 = \theta', \quad (21)$$

$$\alpha^* z_2'(1 - \beta^* z_2^2) + \phi_b [f z_2 - z_1^2] - \frac{1}{\phi_a} K z_1 = 0, \quad (22)$$

$$z_3' \left(1 + \frac{1}{\phi_d} P_r N_r \right) + P_r \frac{\phi_c}{\phi_d} \left[f z_3 - z_1 \theta + \frac{E_L}{\phi_a \phi_c} z_2^2 \right] = 0. \quad (23)$$

$$f(0) = S, z_1(0) = 1 + \Lambda_L z_2(0), z_3(0) = -G_i(1 - \theta(0)), z_1(\infty) \rightarrow 0, \theta(\infty) \rightarrow 0. \quad (24)$$

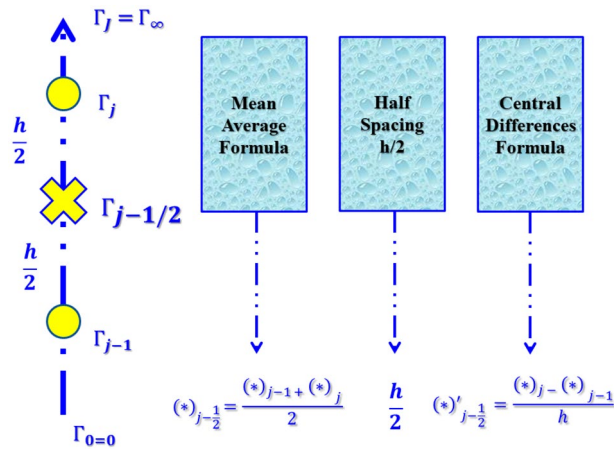


Figure 4. The rectangular grid of difference approximation.

Stage 2: domain discretization. The process domain has to be discretized to compute the estimated solution. Usually, the field is separated into the same grid size by discretization (Fig. 4). The computational findings gain a minor grid relatively with high precision. $\Gamma_0 = 0, \Gamma_j = \Gamma_{j-1} + h, j = 1, 2, 3, \dots, J - 1, \Gamma_J = \Gamma_\infty$. The j is used for providing a h -spacing in a horizontal direction to show the position of the coordinates. The solution is calculated without the use of any initial approximation, so it is essential to measure speed, temperatures, entropy changes, and temperature variations, to make a basic estimation among $\Gamma = 0$ and $\Gamma = \infty$. The obtained designs are approximated solutions provided that they fulfill the criteria of boundary constraints of the problem. It is significant to observe here that the outputs would be equal in the end when different basic estimations are being chosen, but that the iteration count and time are considered to transfer the calculations, which may change (Fig. 3).

Differences formulas are calculated using center differences, and average functions are replaced. The 1st ODEs (19)–(23) order is then reduced to the next series of non-linear algebraic equations.

$$\frac{(z_1)_j + (z_1)_{j-1}}{2} = \frac{f_j - f_{j-1}}{h}, \tag{25}$$

$$\frac{(z_2)_j + (z_2)_{j-1}}{2} = \frac{(z_1)_j - (z_1)_{j-1}}{h}, \tag{26}$$

$$\frac{(z_3)_j + (z_3)_{j-1}}{2} = \frac{\theta_j - \theta_{j-1}}{h}, \tag{27}$$

$$\alpha^* \left(\frac{(z_2)_j - (z_2)_{j-1}}{h} \right) \left(1 - \beta^* \left(\frac{(z_2)_j + (z_2)_{j-1}}{2} \right)^2 \right) + \left[\phi_b \left(\left(\frac{f_j + f_{j-1}}{2} \right) \left(\frac{(z_2)_j + (z_2)_{j-1}}{2} \right) - \left(\frac{(z_1)_j + (z_1)_{j-1}}{2} \right)^2 \right) - K \frac{1}{\phi_a} \left(\frac{(z_1)_j + (z_1)_{j-1}}{2} \right) \right], \tag{28}$$

$$\left(\frac{(z_3)_j - (z_3)_{j-1}}{h} \right) \left(1 + \frac{1}{\phi_d} P_r N_r \right) + P_r \frac{\phi_c}{\phi_d} \left[\left(\frac{f_j + f_{j-1}}{2} \right) \left(\frac{(z_3)_j + (z_3)_{j-1}}{2} \right) - \left(\frac{(z_1)_j + (z_1)_{j-1}}{2} \right) \left(\frac{\theta_j + \theta_{j-1}}{2} \right) \right] + P_r \frac{\phi_c}{\phi_d} \left[\frac{E_L}{\phi_a \phi_c} \left(\frac{(z_2)_j + (z_2)_{j-1}}{2} \right)^2 \right] = 0. \tag{29}$$

Stage 3: linearized formulas by Newton technique. The output formulas are reduced to linearity by applying the Newton technique. The $(i + 1)th$ iteration can be achieved from the application of previous formulas

$$()_j^{(i+1)} = ()_j^{(i)} + \Theta^* ()_j^{(i)}. \tag{30}$$

We get the following linear equation method when we have the above substituted into formulas (25)–(29) and skipped the higher bounds from 2 and more of Π_j^i .

$$\Theta^* f_j - \Theta^* f_{j-1} - \frac{1}{2} h(\Theta^*(z_1)_j + \Theta^*(z_1)_{j-1}) = (r_1)_{j-\frac{1}{2}}, \tag{31}$$

$$\Theta^*(z_1)_j - \Theta^*(z_1)_{j-1} - \frac{1}{2} h(\Theta^*(z_2)_j + \Theta^*(z_2)_{j-1}) = (r_2)_{j-\frac{1}{2}}, \tag{32}$$

$$\Theta^* \theta_j - \Theta^* \theta_{j-1} - \frac{1}{2} h(\Theta^*(z_3)_j + \Theta^*(z_3)_{j-1}) = (r_3)_{j-\frac{1}{2}}, \tag{33}$$

$$(a_1)_j \Theta^* f_j + (a_2)_j \Theta^* f_{j-1} + (a_3)_j \Theta^* z_{1j} + (a_4)_j \Theta^* z_{1j-1} + (a_5)_j \Theta^* z_{2j} + (a_6)_j \Theta^* z_{2j-1} + (a_7)_j \Theta^* \theta_j + (a_8)_j \Theta^* \theta_{j-1} + (a_9)_j \Theta^*(z_3)_j + (a_{10})_j \Theta^*(z_3)_{j-1} = (r_4)_{j-\frac{1}{2}}, \tag{34}$$

$$(b_1)_j \Theta^* f_j + (b_2)_j \Theta^* f_{j-1} + (b_3)_j \Theta^* z_{1j} + (b_4)_j \Theta^* z_{1j-1} + (b_5)_j \Theta^* z_{2j} + (b_6)_j \Theta^* z_{2j-1} + (b_7)_j \Theta^* \theta_j + (b_8)_j \Theta^* \theta_{j-1} + (b_9)_j \Theta^*(z_3)_j + (b_{10})_j \Theta^*(z_3)_{j-1} = (r_5)_{j-\frac{1}{2}}. \tag{35}$$

where

$$(r_1)_{j-\frac{1}{2}} = -f_j + f_{j-1} + \frac{h}{2}(z_1)_j + ((z_1)_{j-1}), \tag{36}$$

$$(r_2)_{j-\frac{1}{2}} = -(z_1)_j + (z_1)_{j-1} + \frac{h}{2}((z_2)_j + (z_2)_{j-1}), \tag{37}$$

$$(r_3)_{j-\frac{1}{2}} = -\theta_j + \theta_{j-1} + \frac{h}{2}((z_3)_j + (z_3)_{j-1}), \tag{38}$$

$$(r_4)_{j-\frac{1}{2}} = -h \left[\alpha^* \left(\frac{(z_2)_j - (z_2)_{j-1}}{h} \right) \left(1 - \beta^* \left(\frac{(z_2)_j + (z_2)_{j-1}}{2} \right)^2 \right) \right] - h \left[\phi_b \left(\frac{f_j + f_{j-1}}{2} \right) \left(\frac{(z_2)_j + (z_2)_{j-1}}{2} \right) - \left(\frac{(z_1)_j + (z_1)_{j-1}}{2} \right)^2 - K \frac{1}{\phi_a} \left(\frac{(z_1)_j + (z_1)_{j-1}}{2} \right) \right], \tag{39}$$

$$(r_5)_{j-\frac{1}{2}} = -h \left[\frac{((z_3)_j - (z_3)_{j-1})}{h} \left(1 + \frac{1}{\phi_d} P_r N_r \right) \right] - h \frac{\phi_c}{\phi_d} P_r \left[\left(\frac{(f_j + f_{j-1})((z_3)_j + (z_3)_{j-1})}{4} \right) \right] + h \frac{\phi_c}{\phi_d} P_r \left[\left(\frac{(\theta_j + \theta_{j-1})((z_1)_j + (z_1)_{j-1})}{4} \right) \right] - h \frac{\phi_c}{\phi_d} P_r \left[\frac{E_L}{\phi_a \phi_c} \left(\frac{(z_2)_j + (z_2)_{j-1}}{2} \right)^2 \right] = 0. \tag{40}$$

The boundary condition becomes

$$\Theta^* f_0 = 0, \Theta^*(z_1)_0 = 0, \Theta^*(z_3)_0 = 0, \Theta^*(z_1)_J = 0, \Theta^* \theta_j = 0. \tag{41}$$

The boundary constraints should be fulfilled even in the event of whole iterations for the completion of the scheme discussed above. So, concern with our actual hypothesis, we apply the limit conditions discussed above for the maintenance of the correct values in each iteration.

Stage 4: the block-tridiagonal array. A tridiagonal-block structure is used in linearized differential formulas (31)–(35). The method is written as follows in a matrix–vector

For $j = 1$;

$$\Theta^* f_1 - \Theta^* f_0 - \frac{1}{2} h(\Theta^*(z_1)_1 + \Theta^*(z_1)_0) = (r_1)_{1-\frac{1}{2}}, \tag{42}$$

$$\Theta^*(z_1)_1 - \Theta^*(z_1)_0 - \frac{1}{2} h(\Theta^*(z_2)_1 + \Theta^*(z_2)_0) = (r_2)_{1-\frac{1}{2}}, \tag{43}$$

$$\Theta^* \theta_1 - \Theta^* \theta_0 - \frac{1}{2} h(\Theta^*(z_3)_1 + \Theta^*(z_3)_0) = (r_3)_{1-\frac{1}{2}}, \tag{44}$$

$$(a_1)_1 \Theta^* f_1 + (a_2)_1 \Theta^* f_0 + (a_3)_1 \Theta^* z_{11} + (a_4)_1 \Theta^* z_{10} + (a_5)_1 \Theta^* z_{21} + (a_6)_1 \Theta^* z_{20} + (a_7)_1 \Theta^* \theta_j + (a_8)_1 \Theta^* \theta_0 + (a_9)_1 \Theta^*(z_3)_1 + (a_{10})_1 \Theta^*(z_3)_0 = (r_4)_{1-\frac{1}{2}}, \tag{45}$$

$$(b_1)_1 \Theta^* f_1 + (b_2)_1 \Theta^* f_0 + (b_3)_1 \Theta^* z_{11} + (b_4)_1 \Theta^* z_{10} + (b_5)_1 \Theta^* z_{21} + (b_6)_1 \Theta^* z_{20} + (b_7)_1 \Theta^* \theta_1 + (b_8)_1 \Theta^* \theta_0 + (b_9)_1 \Theta^* (z_3)_1 + (b_{10})_1 \Theta^* (z_3)_0 = (r_5)_{1-\frac{1}{2}}. \tag{46}$$

In array arrangement,

$$\begin{bmatrix} 0 & 0 & 1 & 0 & 0 \\ -h/2 & 0 & 0 & -h/2 & 0 \\ 0 & -h/2 & 0 & 0 & -h/2 \\ (a_2)_1 & (a_{10})_1 & (a_3)_1 & (a_1)_1 & (a_9)_1 \\ (b_2)_1 & (b_{10})_1 & (b_3)_1 & (b_1)_1 & (b_9)_1 \end{bmatrix} \begin{bmatrix} \Theta^*(z_2)_0 \\ \Theta^*(\theta)_0 \\ \Theta^*(f)_1 \\ \Theta^*(z_2)_1 \\ \Theta^*(z_3)_1 \end{bmatrix} + \begin{bmatrix} -h/2 & 0 & 0 & 0 & 0 \\ 1 & 0 & 0 & 0 & 0 \\ 0 & 1 & 0 & 0 & 0 \\ (a_5)_1 & (a_7)_1 & 0 & 0 & 0 \\ (b_5)_1 & (b_7)_1 & 0 & 0 & 0 \end{bmatrix} \begin{bmatrix} \Theta^*(z_1)_1 \\ \Theta^*(\theta)_1 \\ \Theta^*(f)_2 \\ \Theta^*(z_2)_2 \\ \Theta^*(z_3)_2 \end{bmatrix} = \begin{bmatrix} (r_1)_{\frac{1}{2}} \\ (r_2)_{\frac{1}{2}} \\ (r_3)_{\frac{1}{2}} \\ (r_4)_{\frac{1}{2}} \\ (r_5)_{\frac{1}{2}} \end{bmatrix}. \tag{47}$$

That is

$$[A_1][\Theta_1^*] + [C_1][\Theta_2^*] = [r_1]. \tag{48}$$

For $j = 2$;

$$\Theta^* f_2 - \Theta^* f_1 - \frac{1}{2} h(\Theta^*(z_1)_2 + \Theta^*(z_1)_1) = (r_1)_{1-\frac{1}{2}}, \tag{49}$$

$$\Theta^*(z_1)_2 - \Theta^*(z_1)_1 - \frac{1}{2} h(\Theta^*(z_2)_2 + \Theta^*(z_2)_1) = (r_2)_{1-\frac{1}{2}}, \tag{50}$$

$$\Theta^* \theta_1 - \Theta^* \theta_0 - \frac{1}{2} h(\Theta^*(z_3)_2 + \Theta^*(z_3)_1) = (r_3)_{1-\frac{1}{2}}, \tag{51}$$

$$(a_1)_2 \Theta^* f_2 + (a_2)_2 \Theta^* f_1 + (a_3)_2 \Theta^* z_{12} + (a_4)_2 \Theta^* z_{11} + (a_5)_2 \Theta^* z_{22} + (a_6)_2 \Theta^* z_{21} + (a_7)_2 \Theta^* \theta_2 + (a_8)_2 \Theta^* \theta_1 + (a_9)_2 \Theta^* (z_3)_2 + (a_{10})_2 \Theta^* (z_3)_1 = (r_4)_{2-\frac{1}{2}}, \tag{52}$$

$$(b_1)_2 \Theta^* f_2 + (b_2)_2 \Theta^* f_1 + (b_3)_2 \Theta^* z_{12} + (b_4)_2 \Theta^* z_{11} + (b_5)_2 \Theta^* z_{22} + (b_6)_2 \Theta^* z_{21} + (b_7)_2 \Theta^* \theta_2 + (b_8)_2 \Theta^* \theta_1 + (b_9)_2 \Theta^* (z_3)_2 + (b_{10})_2 \Theta^* (z_3)_1 = (r_5)_{2-\frac{1}{2}}. \tag{53}$$

In array arrangement,

$$\begin{bmatrix} 0 & 0 & -1 & 0 & 0 \\ 0 & 0 & 0 & -h/2 & 0 \\ 0 & 0 & 0 & 0 & -h/2 \\ 0 & 0 & (a_4)_2 & (a_2)_2 & (a_{10})_2 \\ 0 & 0 & (b_4)_2 & (b_2)_2 & (b_{10})_2 \end{bmatrix} \begin{bmatrix} \Theta^*(z_2)_0 \\ \Theta^*(\theta)_0 \\ \Theta^*(f)_1 \\ \Theta^*(z_2)_1 \\ \Theta^*(z_3)_1 \end{bmatrix} + \begin{bmatrix} -h/2 & 0 & 1 & 0 & 0 \\ -1 & 0 & 0 & -h/2 & 0 \\ 0 & -1 & 0 & 0 & -h/2 \\ (a_6)_2 & (a_8)_2 & (a_3)_2 & (a_1)_2 & (a_9)_2 \\ (b_6)_2 & (b_8)_2 & (b_3)_2 & (b_1)_2 & (b_9)_2 \end{bmatrix} \begin{bmatrix} \Theta^*(z_1)_1 \\ \Theta^*(\theta)_1 \\ \Theta^*(f)_2 \\ \Theta^*(z_2)_2 \\ \Theta^*(z_3)_2 \end{bmatrix} + \begin{bmatrix} -h/2 & 0 & 1 & 0 & 0 \\ 1 & 0 & 0 & -h/2 & 0 \\ 0 & 1 & 0 & 0 & -h/2 \\ (a_5)_2 & (a_7)_2 & 0 & 0 & 0 \\ (b_5)_2 & (b_7)_2 & 0 & 0 & 0 \end{bmatrix} \begin{bmatrix} \Theta^*(z_1)_1 \\ \Theta^*(\theta)_1 \\ \Theta^*(f)_2 \\ \Theta^*(z_2)_2 \\ \Theta^*(z_3)_2 \end{bmatrix} = \begin{bmatrix} (r_1)_{\frac{3}{2}} \\ (r_2)_{\frac{3}{2}} \\ (r_3)_{\frac{3}{2}} \\ (r_4)_{\frac{3}{2}} \\ (r_5)_{\frac{3}{2}} \end{bmatrix}. \tag{54}$$

That is

$$[B_2][\Theta_1^*] + [A_2][\Theta_2^*] + [C_2][\Theta_3^*] = [r_2]. \tag{55}$$

For $j = J - 1$;

$$\Theta^* f_{J-1} - \Theta^* f_{J-2} - \frac{1}{2} h(\Theta^*(z_1)_{J-1} + \Theta^*(z_1)_{J-2}) = (r_1)_{J-1-\frac{1}{2}}, \tag{56}$$

$$\Theta^*(z_1)_{J-1} - \Theta^*(z_1)_{J-2} - \frac{1}{2} h(\Theta^*(z_2)_{J-1} + \Theta^*(z_2)_{J-2}) = (r_2)_{J-1-\frac{1}{2}}, \tag{57}$$

$$\Theta^* \theta_{J-1} - \Theta^* \theta_{J-2} - \frac{1}{2} h(\Theta^*(z_3)_{J-1} + \Theta^*(z_3)_{J-2}) = (r_3)_{J-1-\frac{1}{2}}, \tag{58}$$

$$(a_1)_{J-1} \Theta^* f_{J-1} + (a_2)_{J-1} \Theta^* f_{J-2} + (a_3)_{J-1} \Theta^* z_{1J-1} + (a_4)_{J-1} \Theta^* z_{1J-2} + (a_5)_{J-1} \Theta^* z_{2j} + (a_6)_{J-1} \Theta^* z_{2J-2} + (a_7)_{J-1} \Theta^* \theta_{J-1} + (a_8)_{J-1} \Theta^* \theta_{J-2} + (a_9)_{J-1} \Theta^* (z_3)_{J-1} + (a_{10})_{J-1} \Theta^* (z_3)_{J-2} = (r_4)_{J-1-\frac{1}{2}}, \tag{59}$$

P_r	Ref. ⁵⁴	Ref. ⁵⁵	Ref. ⁵⁶	Ref. ⁵⁷	Present
72×10^{-2}	08086×10^{-4}	08086×10^{-4}	080863135×10^{-8}	080876122×10^{-8}	080876181×10^{-8}
1×10^0	1×10^0	1×10^0	1×10^0	1×10^0	1×10^0
3×10^0	$19,237 \times 10^{-4}$	$19,236 \times 10^{-4}$	$192,368,259 \times 10^{-8}$	$192,357,431 \times 10^{-8}$	$192,357,420 \times 10^{-8}$
7×10^0	$30,723 \times 10^{-4}$	$30,722 \times 10^{-4}$	$307,225,021 \times 10^{-8}$	$307,314,679 \times 10^{-8}$	$307,314,651 \times 10^{-8}$
10×10^0	$37,207 \times 10^{-4}$	$37,006 \times 10^{-4}$	$372,067,390 \times 10^{-8}$	$372,055,436 \times 10^{-8}$	$372,055,429 \times 10^{-8}$

Table 4. Comparing of $-\theta'(0)$ values with P_r , when $\phi = 0$, $\phi_{hnf} = 0$, $E_L = 0$, $\Lambda_L = 0$, $N_L = 0$, $S = 0$ and $G_L = 0$.

Here R increases the $J \times J$ tridiagonal block array for all heavy sizes of 5×5 , while, Θ^* and p are $J \times 1$ order columns vector. The factorization method LU is applied to obtain the Θ^* solution. Array R must be selected in a way that provides us a nonsingular matrix such that factoring can be done easily. Whereas $R\Theta^* = p$ works on the vector directly to the tridiagonal block array R , to generate another vector p . The tridiagonal R factorization bulk is extra classified into the triangular matrices lower and upper, i.e., $R = LU$ can be expressed as $LU\Theta^* = p$, so let $U\Theta^* = y$ generates $Ly = p$, which provides y solution is once again connected into $U\Theta^* = y$ to answer for Θ^* . Since we deal with triangular arrays, replacing is the path forward.

Code verification

On the other, by measuring the heat transmission rate outcomes from the current technique against the recent results available in the literature^{54–57}, the method's validity was evaluated. Table 4 summarises the comparing of reliabilities current during the researches. Nevertheless, the outcomes of the current examination are exceedingly accurate.

The strategy of finite differences was adopted by Ishak et al.^{54,55} to explore the solution of the model considered. The entropy study by HAM (homotopy analysis method) for time-dependent magneto-nanofluid was proposed by Abolbashari et al.⁵⁶ (HAM). Das et al.⁵⁷ resolved with the RK Fehlberg technique the unsteadiness status of the controlling formulas. Compared to previous ones, KBM applied here provides very precise performance.

Entropy analysis

Porous media generally increase the entropy of the system^{58–61} described the nanofluid entropy production by:

$$E_G = \frac{k_{hnf}}{\mathbb{Y}_\infty^2} \left\{ \left(\frac{\partial \mathbb{Y}}{\partial y} \right)^2 + \frac{16}{3} \frac{\sigma^* \mathbb{Y}_\infty^3}{\kappa^* \nu_f (\rho C_p)_f} \left(\frac{\partial \mathbb{Y}}{\partial y} \right)^2 \right\} + \frac{\mu_{hnf}}{\mathbb{Y}_\infty} \left(\frac{\partial v_1}{\partial y} \right)^2 + \frac{\mu_{hnf} v_1^2}{k \mathbb{Y}_\infty}. \quad (72)$$

The non-dimensional formulation of entropy analysis is as follows^{62–66}

$$N_G = \frac{\mathbb{Y}_\infty^2 b^2 E_G}{k_f (\mathbb{Y}_w - \mathbb{Y}_\infty)^2}. \quad (73)$$

By formula (9), the non-dimensional entropy formula is:

$$N_G = Re \left[\phi_d (1 + N_r) \theta'^2 + \frac{1}{\phi_a} \frac{B_r}{\Omega} (f''^2 + K f'^2) \right], \quad (74)$$

Here $Re = \frac{U_w b^2}{\nu_f x}$ is the Reynolds number, $B_r = \frac{\mu_f U_w^2}{k_f (\mathbb{Y}_w - \mathbb{Y}_\infty)}$ signifies the Brinkman amount and $\Omega = \frac{w - \mathbb{Y}_\infty}{\mathbb{Y}_\infty}$ symbols the dimensionless gradient of the temperature.

Results and discussion

The following discussion is based on the numerical results obtained from the model mentioned in the last part. The potential parameters α^* , β^* , K , ϕ , $\Lambda_L S$, E_L , N_L , G_L , R_L and B_L are assumed in this section. These variables reveal the physical aspects, including, swiftness, temperature, and entropy, of the dimensionless values in Figs. 5, 6, 7, 8, 9, 10, 11 and 12. For Cu–EO trivial P-ENF and MoS₂–Cu/EO non-Newtonian P-EHNF, the results are extracted. Table 5 demonstrates the drag force coefficients and temperature change. The extra values were $\alpha^* = 1.0$, $\beta^* = 0.4$, $K = 0.1$, $\phi = 0.18$, $\phi_{Ms} = 0.09$, $\Lambda_L = 0.3$, $S = 0.4$, $N_L = 0.3$, $E_L = 0.3$, $G_L = 0.3$, $R_L = 5$ and $B_L = 5$. In order to have insight into the physical problem, these results are debated concisely in the following subsection.

Influence of Prandtl–Eyring parameter α^* . The impact of α^* towards the velocity of the hybrid nanofluid has been clearly shown in Fig. 5a. It is noted that amplify α^* will quicken further the velocity motion. The physical motivation behind this phenomenon is the α^* causes deterioration in viscosity of the fluid where the resistance will lessening and instead upsurge the velocity of the fluid. Furthermore, the MoS₂–Cu/EO has a greater thickness of boundary layer flow as compared to Cu–EO. The physical intention is the nanofluid devising a higher density influence compared to the hybrid nanofluid. In contrast, the temperature profile of the flow exposed declining manner as α^* enlarge, which has been depicted in Fig. 5b. The triggered of this decreased

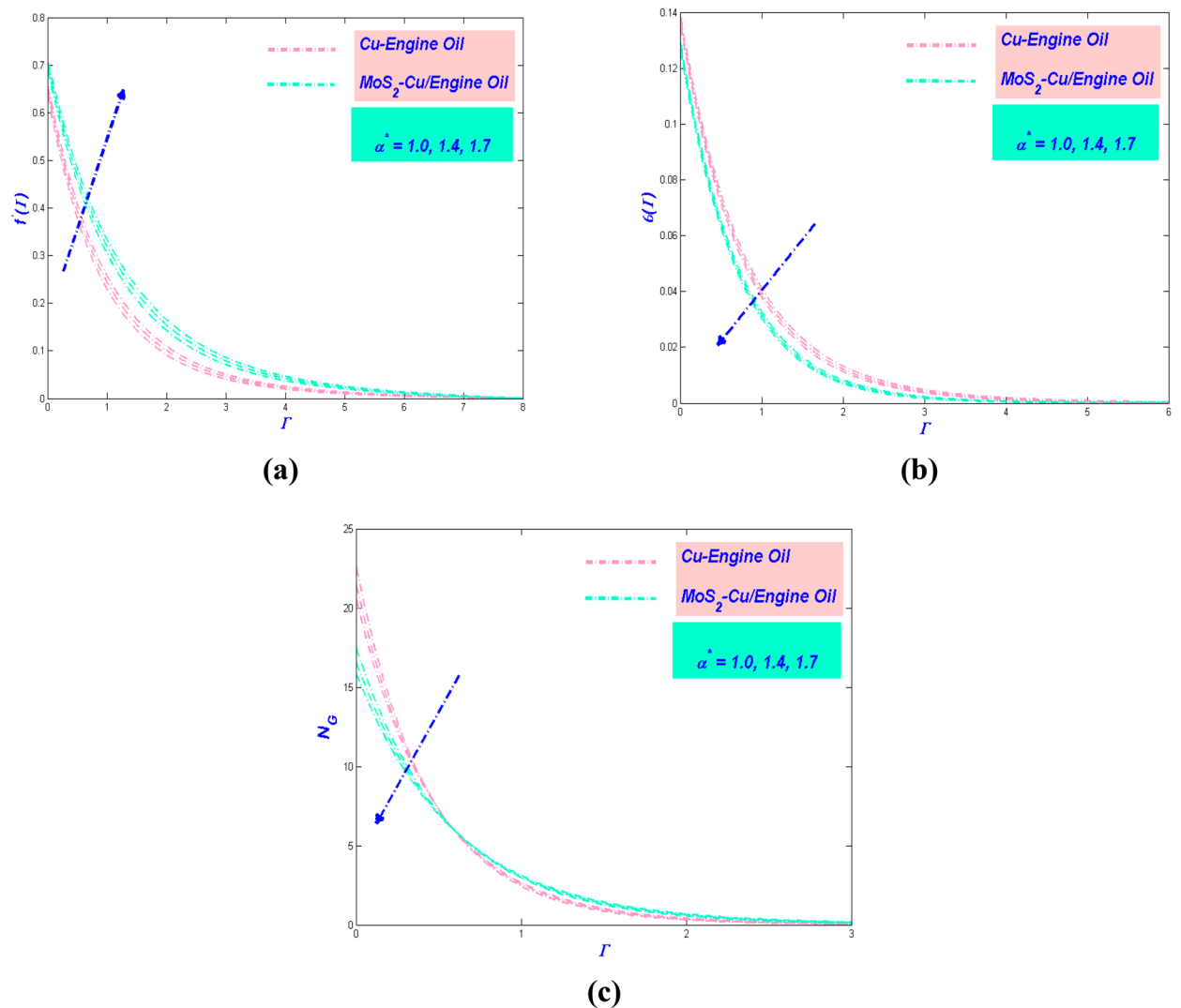


Figure 5. (a) Velocity, (b) temperature and (c) entropy variation versus α^* .

manner due to the velocity intensifications, and more heat can be transmitted faster. It is also being noticed that $\text{MoS}_2\text{-Cu/EO}$ has a lower temperature compared to Cu-EO . It is because the hybrid nanofluid has a lower thermal conductivity in comparison with nanofluid. It is worth considering the entropy variation in the influence of α^* . Figure 5c illustrates the entropy reduced as α^* augmented. The reason behind this phenomenon is the hybrid nanofluid motion diminution due to lower temperature, which will distress the entropy of the system reduction. Moreover, as the heat transfer rate increases in Table 5, the thermal efficiency of PTSC will improve in a solar water pump.

Influence of Prandtl–Eyring parameter β^* . The actions of the fluid velocity by the effect of β^* being exposed in Fig. 6a. The figure reveals the velocity subsidence as β^* proliferate. It is well known that β^* varies inversely with the momentum diffusivity and β^* also brings resistance to the hybrid nanofluid particle. Hence, β^* will diminish the velocity of the flow. It is noticeable that Cu-EO has deficient speed compared to $\text{MoS}_2\text{-Cu/EO}$. The density of Cu-EO is thicker than $\text{MoS}_2\text{-Cu/EO}$, which makes the flow arduous to move. Moreover, Fig. 6b portrayed the variation of temperature with the implementation of β^* . It is apparent from the figure that the temperature boost as β^* surge. The circumstance happens attributable to the flow velocity cutback; hence there has been depreciation in transmitting the heat from the surface. Therefore, the entropy of the system will intensify, as adorned in Fig. 6c. β^* magnified the hindrance in the system, as a result, the entropy of the system growth.

Effect of porous media variable K . The aftermath of K beneficial to the velocity of the flow exhibited in Fig. 7a. The velocity depreciated when K upsurged. It is acknowledged that the porosity will make the fluid flow pathway being separated hence shrinkage the velocity of the flow. In other words, the porosity will become an obstruction to the flow. The reduction of velocity will always be allied to temperature demeanor. Figure 7b

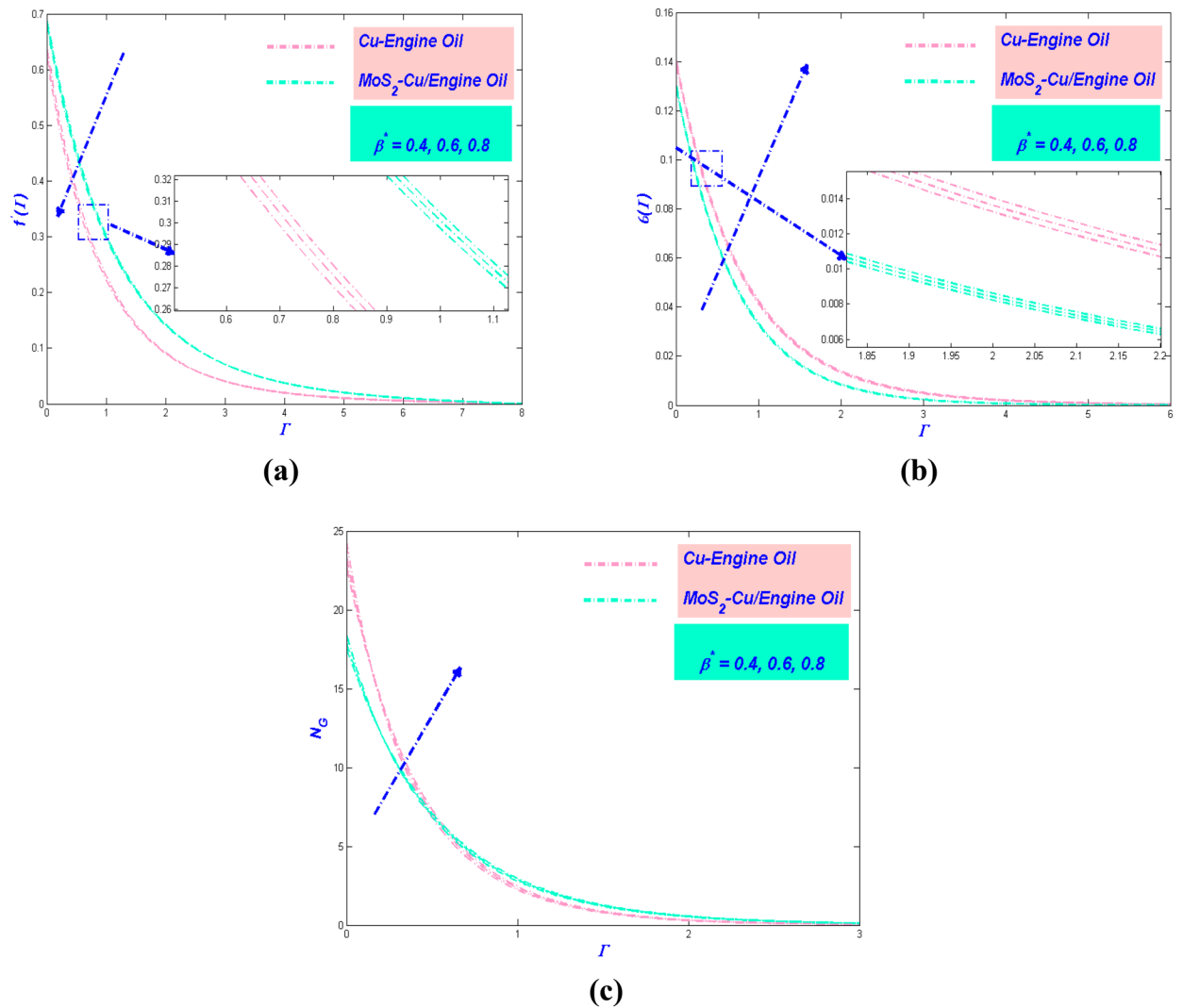


Figure 6. (a) Velocity, (b) temperature and (c) entropy variation versus β^* .

exemplifies the consequence of K concerning the temperature of the flow. The temperature is seen to augment as K raise. The trend, as mentioned earlier detected in Fig. 7c. The same explanation is established for this behavior. The entropy of the system will be inflation as K increased (Fig. 7c). This action cannot be avoided since the temperature profile is pictured as dilated. It is perceptible that the entropy for Cu-EO is quite similar to MoS₂-Cu/EO. This anomaly occurs because the size of molecule hybrid and non-hybrid nanofluid is equivalent to each other.

Effect of nanomolecules size ϕ and ϕ_{hnf} . The consequence of the nano molecules size regarding velocity, temperature, and entropy profile is worth to be discussed. The numerical results for velocity variation are pointed out in Fig. 8a. The velocity is waring as the nano molecule size aggrandize. This decency takes place due to the surface area of the nano particles will be enhanced, and afterward, the density of hybrid nanofluid will be increased. Hence, it will produce a decline in the flow velocity. A noticeable, MoS₂-Cu/EO has the greatest speed value when the size of nano molecules is so small. Hence, this showed that the dispersion of nano molecules would be optimum when the size is small enough. As seen in Fig. 8b, the temperature of the flow rises as the nano molecule size upsurge. The decline in the nano molecule size will make the nano molecules diffuse in the far-field flow because of the temperature difference. It will cause an increment in the thickness of the thermal boundary layer. The minimum value of the size of nano molecules invented that it can be used to produce the lowest temperature profile. The variation of the entropy obliging the nano molecule size is delineated in Fig. 8c. It indicated that the rise of nano molecule size would escalate the entropy profile. The entropy of Cu-EO is higher than MoS₂-Cu/EO due to the hybrid nanofluid has a large amount of thermal conductivity as compared to the nanofluid.

Effect of velocity slip variable Λ_L . Figure 9a embossed the velocity slip notorious the velocity of the flow. It is exposed that the velocity slip makes the velocity declining. It is expected that the velocity slip can create

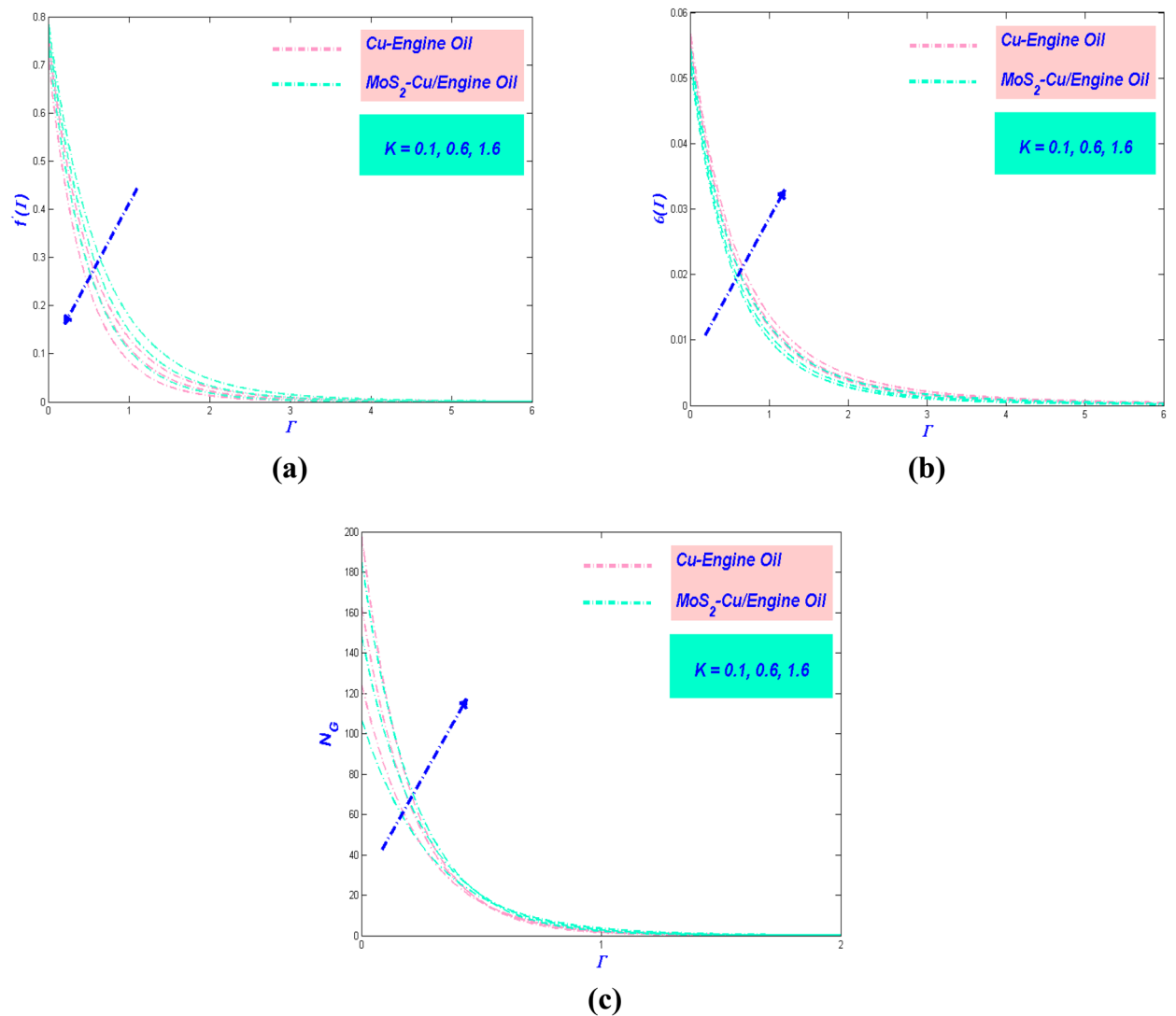


Figure 7. (a) Velocity, (b) temperature, and (c) entropy change with K .

more disturbance and deaccelerate the fluid motion. In the physical sense, when the velocity slip is increased, the far-field velocity flow shows a decreasing behaviour; so, the applied forces to pull the stretching surface are reduced and cannot transfer the energy to the fluid. However, it is observed that MoS₂-Cu/EO has the maximum velocity as compared to Cu-EO because of their significance in thermophysical properties of hybrid nanofluid. The temperature profile will be affected by the changes made by the velocity profile. Figure 9b illustrated the difference in the demeanor of temperature when velocity slips acting on the system. The depreciation of velocity will have affected the viscosity of the boundary layer to be more viscous. Hence it will have magnified the temperature of the flow. It is expected to see that the temperature of MoS₂-Cu/EO is the lowest than Cu-EO since the hybrid nanofluid has less viscosity than the conventional nanofluid. However, a different case happens to the entropy variation for the effect of velocity slip. As seen in Fig. 9c, the entropy of the system abatement as the increment of velocity slips. These results are also being agreed by Turkyilmazoglu⁶⁷.

Thermal radiative variable N_r influence. Thermal radiation is significant because the basic factor that affects the temperature of the earth as a whole is balancing the heat difference between the coming solar radiations and the earth's outgoing thermal radiation. The increment of the thermal radiative variable will enhance the temperature variation, as depicted in Fig. 10a. In the physical sense, this increment can be justified by assuming the thermal radiation converse into electromagnetic energy, and as a result, the distance of radiate from the surface increases, which will eventually raise the temperature of the boundary layer flow. Hence, the thermal radiative variable plays a crucial role to check the temperature profile of the system. It is also beneficial to observe the performance of entropy with the repercussion of the thermal radiative variable. Figure 10b embellished the augmentation of the entropy in the interest of strengthening the thermal radiative variable. The reasoning for this happening by the goodness of the existence of the irreparable nature of the heat transfer that takes place in

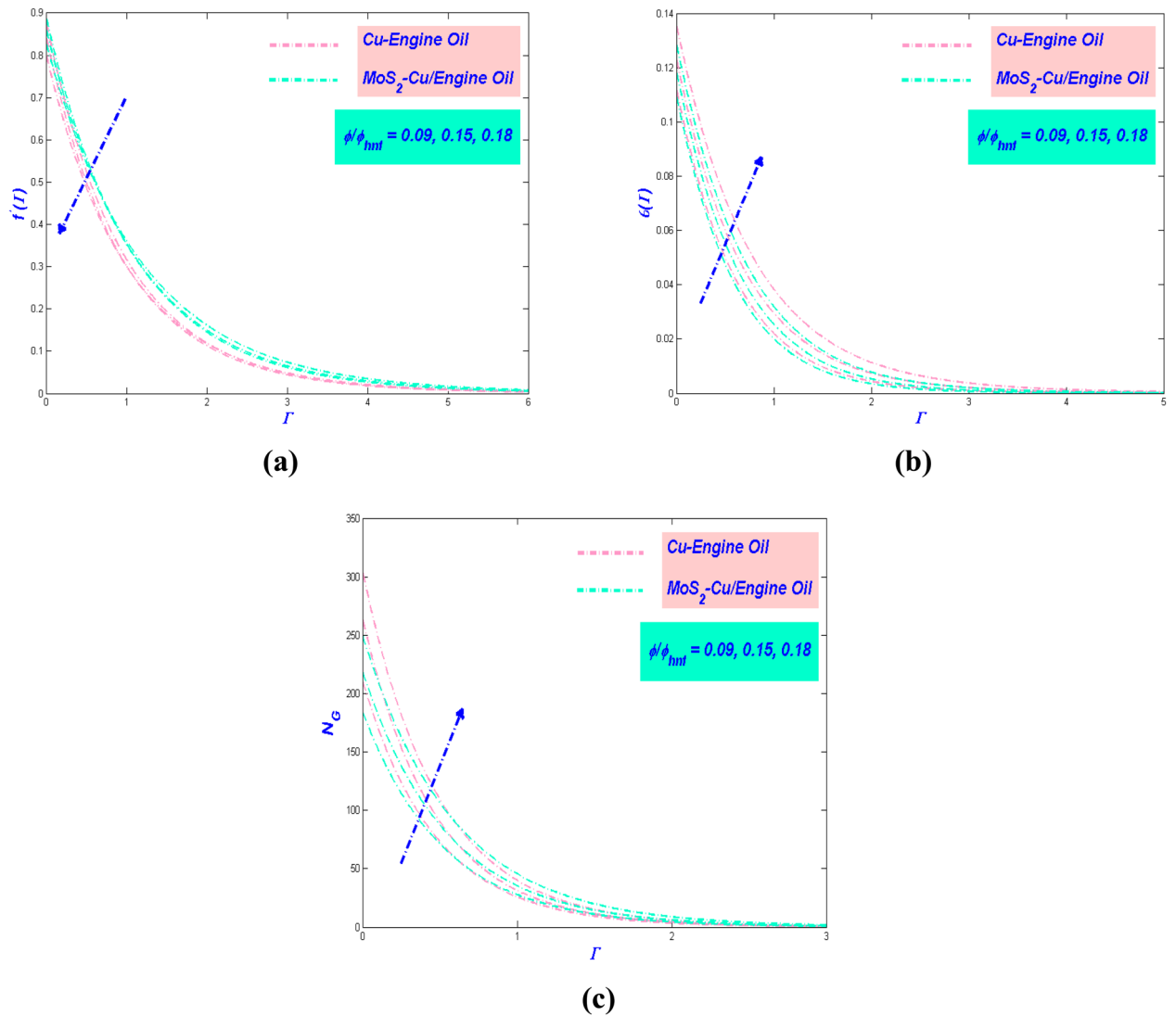


Figure 8. (a) Velocity, (b) temperature and (c) entropy versus ϕ and ϕ_{hmf} .

the system. Also, the increasing behaviour of the Nusselt number Table 5 will cause to increase in the thermal efficacy and performance of PTSC in SWP.

Effect of Eckert number E_L . The Eckert number E_L constantly referring to the kinetic energy of the fluid enthalpy. Based on Fig. 11a, the increment of E_L influenced the temperature profile to upsurge. This behavior arises cause of the action of dissipation which will involve the internal friction of the flow. Further, it will cause self-heating and enhance the temperature of the system. The temperature variation for MoS₂-Cu/EO has a lower value than Cu-EO due to its physical properties. Meanwhile, the entropy of the system showed increment when E_L boost up, as shown in Fig. 11b. Entropy production effect of increasing E_L is evident at the stretched sheet surface. However, in the central flow zone, it does not have a significant influence. Still, the hybrid nanofluid has the lowest entropy in the system. Furthermore, as the heat transfer rate increases in Table 5, the thermal efficiency of PTSC will improve in SWP.

R_e and B_r influences on entropy rate. It is meaningfulness to point the efficacy of the Reynolds number propitious the fluid flow. It is widely known that can directly affect entropy production. This evidence can be shown in Fig. 12a, which showed the amplify of makes the entropy generation augmentation further. This twist is because of augmentation in fluid friction and the thermal boundary layer thickness. This will also create a disturbance in the fluid flow and changes the flow into disorganization. Figure 12b details the entropy profile fluctuation against the Brinkman number's multiple values. The number of Brinkman is the difference between heat energy produced by the transmission of molecules with the feature of viscous dislocation and heat. Theoretically, the dominant aspect in the heat produced by viscous dislocation causes a decline for the growing values of Brinkman numbers, which leads to an augmentation in the rate of entropy generation.

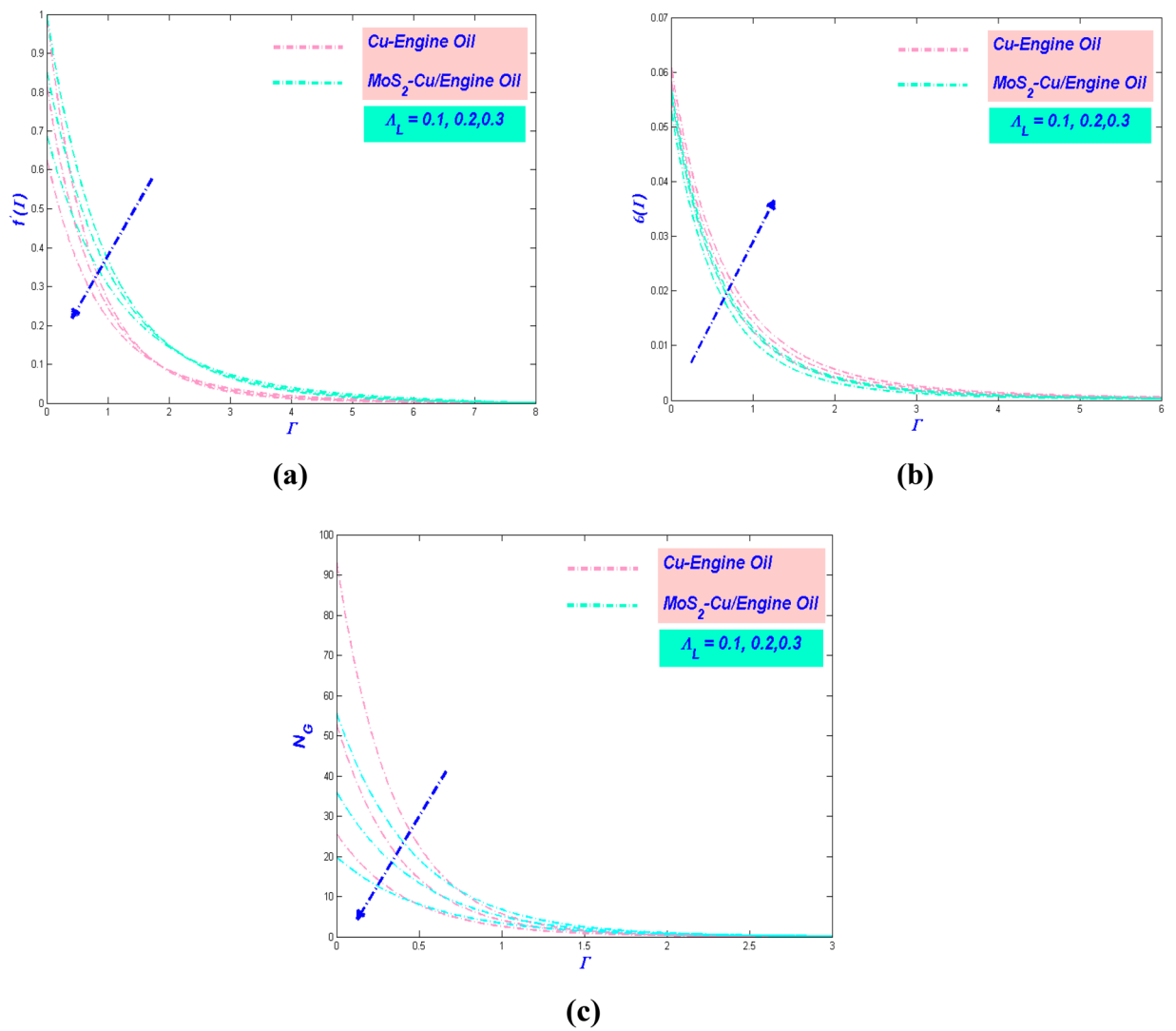


Figure 9. (a) Velocity, (b) temperature and (c) entropy variations with Λ_L .

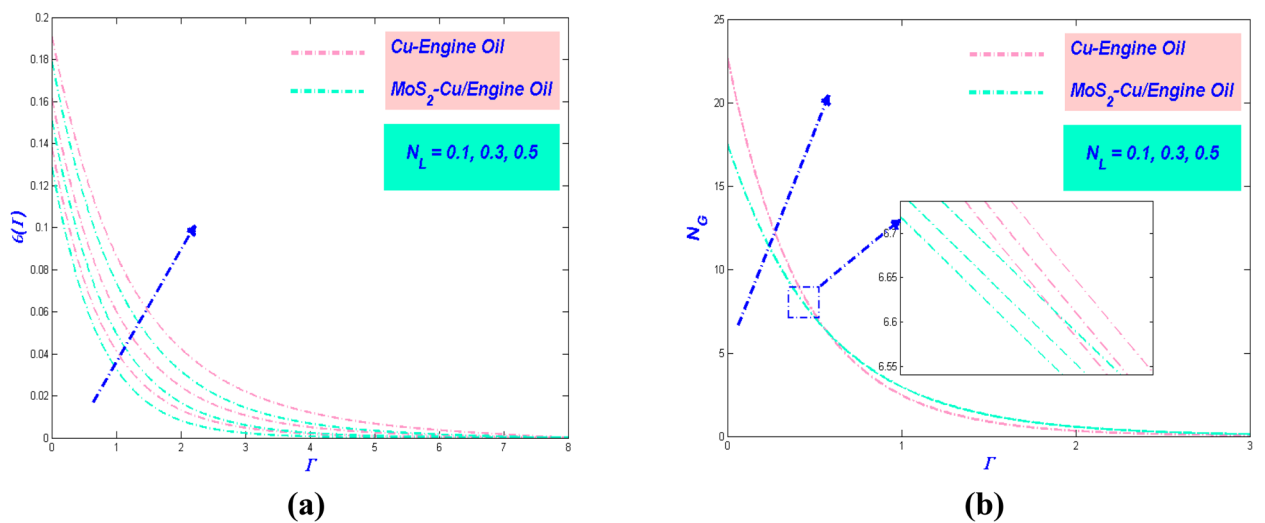


Figure 10. (a) Temperature and (b) entropy variations versus N_L .

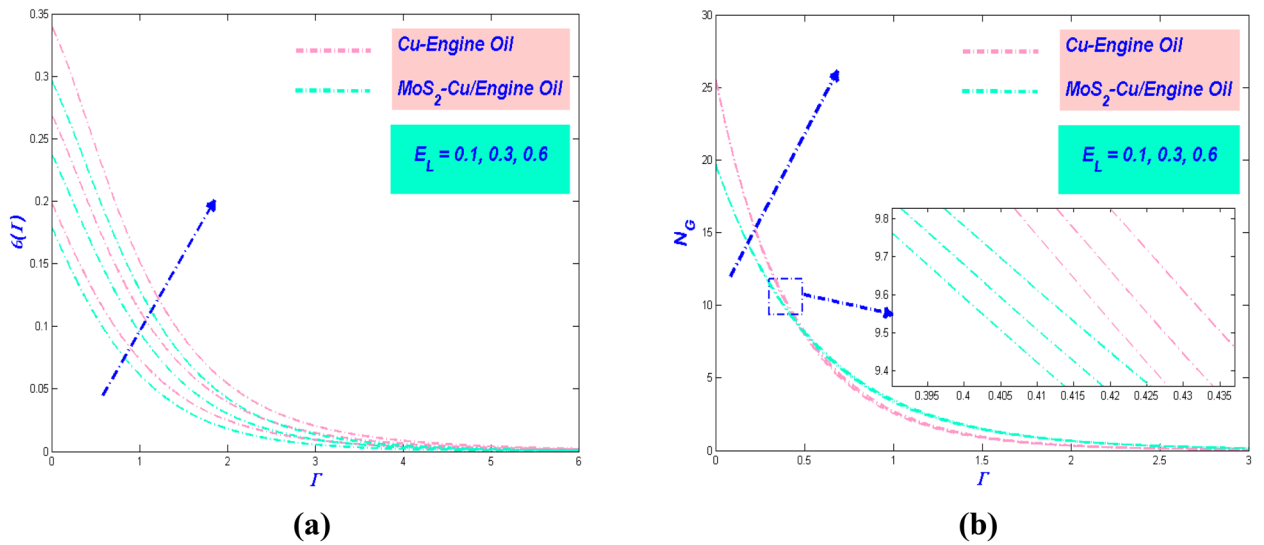


Figure 11. (a) Temperature and (b) entropy variations with E_L .

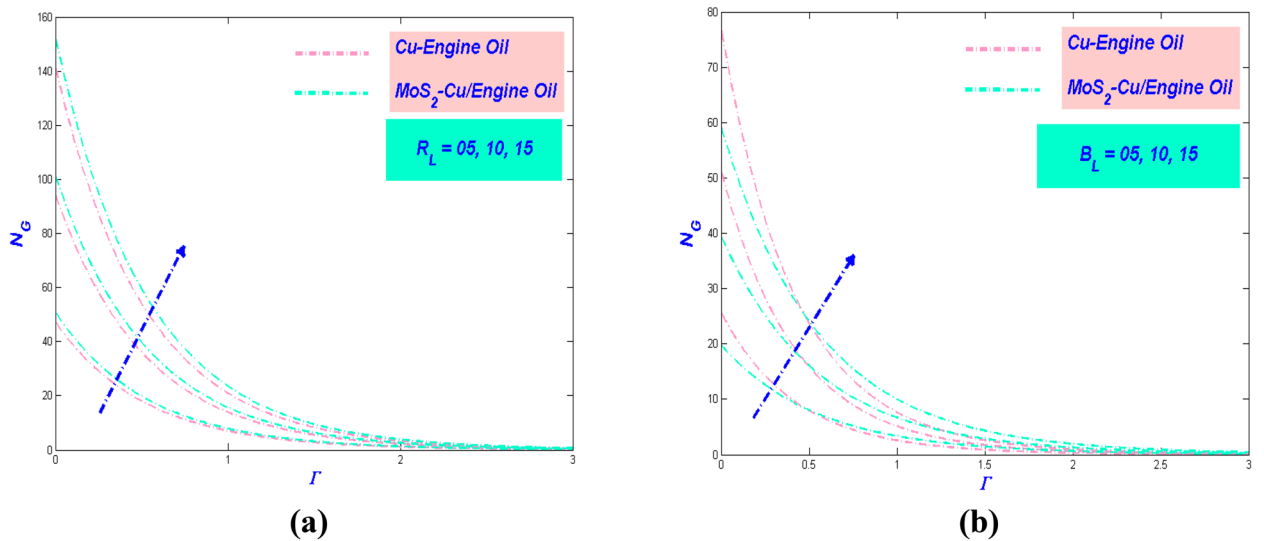


Figure 12. Entropy variations versus (a) R_e and (b) B_r .

In the engineering interest, the numerical values of some physical quantities of different values of the pertinent parameters are shown in Table 5. It is perceived that the skin friction coefficient $C_f Re_x^{1/2}$ aggrandize as the increment of α^* , K , ϕ , ϕ_{Ms} and S parameters. Unfortunately, the enhanced β^* and Λ_L parameters affected $C_f Re_x^{1/2}$ to depreciate. On the other hand, the relative local Nusselt number $Nu_x Re_x^{-1/2}$ (in percentage) for hybrid nanofluid demonstrated an intensify with the rise of α^* , β^* , K and Λ_L parameters. While the ϕ , ϕ_{Ms} , S , N_L , G_L and E_L displayed the deteriorate of the relative $Nu_x Re_x^{-1/2}$.

Final results and future guidance

The main purpose of this research is to discuss the behaviours of controlling parameters consisting of Prandtl–Eyring, permeable media, size of nano molecule particles, velocity slip, thermal radiative variable, Biot number, Eckert number, Reynolds number, and Brinkman number on the efficiency of the PTSC water pump MoS_2-Cu/EO and $Cu-EO$ hybrid/nanofluid. The efficiency of SWP is discussed, by making a decline in the flow of hybrid nanofluid MoS_2-Cu/EO and single nanofluid $Cu-EO$, along with the description of heat transfer. The mathematical formulation is converted into ordinary differential equations by applying an appropriate similarity transformation. Then the system of converted ordinary differential equations is solved using Keller Box Scheme, and the extracted results can be described as follows:

- Only augmented the fluid velocity, whereas parameters reduce the fluid acceleration.
- The parameters increase the temperature of hybrid nanofluid MoS_2-Cu/EO and single nanofluid $Cu-EO$.

α^*	β^*	K	ϕ	ϕ_{Ms}	Λ_L	S	N_L	G_L	E_L	$C_f Re_x^{1/2}$ Cu-EO	$C_f Re_x^{1/2}$ MoS ₂ -Cu/ EO	$Nu_x Re_x^{-1/2}$ Cu-EO	$Nu_x Re_x^{-1/2}$ MoS ₂ -Cu/EO	Relative % $\frac{Nu_{(Ms-Cu/EO)} - Nu_{(Cu)}}{Nu_{(Ms-Cu/EO)}}$
1.0	0.4	0.1	0.18	0.09	0.3	0.4	0.3	0.3	0.3	4.3045	5.1062	3.7097	3.8554	3.7%
1.4										4.3320	5.1316	3.7363	3.8903	3.9%
1.7										4.3517	5.1601	3.7523	3.9245	4.3%
	0.4									4.3045	5.1062	3.7097	3.8554	3.7%
	0.6									4.2825	5.0988	3.6712	3.8320	4.1%
	0.8									4.2571	5.0221	3.6542	3.8163	4.2%
		0.1								4.3045	5.1062	3.7097	3.8554	3.7%
		0.6								4.3390	5.1336	3.7215	3.8871	4.2%
		1.6								4.3551	5.1754	3.7563	3.9282	4.3%
			0.09							4.2436	-	3.6484	-	-
			0.15							4.2809	-	3.6796	-	3.6%
			0.18							4.3045	-	3.7097	-	3.7%
				0.0						-	4.2436	-	3.6484	-
				0.06						-	5.0926	-	3.8207	3.6%
				0.09						-	5.1062	-	3.8554	3.7%
					0.1					4.3534	5.1288	3.7616	3.8954	3.4%
					0.2					4.3382	5.1163	3.7325	3.8711	3.5%
					0.3					4.3045	5.1062	3.7097	3.8554	3.7%
						0.2				4.2715	5.0958	3.6752	3.8235	3.8%
						0.4				4.3045	5.1062	3.7097	3.8554	3.7%
						0.6				4.3260	5.1266	3.7235	3.8831	4.1%
							0.1			4.3045	5.1062	3.6831	3.8167	3.5%
							0.3			4.3045	5.1062	3.7097	3.8554	3.7%
							0.5			4.3045	5.1062	3.7243	3.8895	4.2%
								0.1		4.3045	5.1062	3.6720	3.8040	3.4%
								0.3		4.3045	5.1062	3.7097	3.8554	3.7%
								0.5		4.3045	5.1062	3.7234	3.8959	4.4%
									0.1	4.3045	5.1062	3.6811	3.8105	3.3%
									0.3	4.3045	5.1062	3.7097	3.8554	3.7%
									0.6	4.3045	5.1062	3.7402	3.8978	4.0%

Table 5. Values of $C_f Re_x^{1/2}$ and $Nu_x Re_x^{-1/2}$ for $Pr = 6450$.

- The entropy production increases when the effect of parameters is acting on the system. Besides, the effect of parameters reduces the rate of entropy generation.
- By uplifting the parameters of the skin friction coefficient was increased. However, parameters reduce the rate of skin friction coefficient.
- Increase in the parameters resulted in an increment of heat transfer rate, whereas the same variation was reduced due to the effect of Prandtl–Eyring and velocity slippery parameters.
- The thermal efficiency range of MoS₂-Cu/EO over Cu-EO is from the minimal rate of and maximized up to.

For further investigation, additional factors such as the superior chemical and thermal criticality must be included in the flow behavior at large values of the thermal conductivity parameter. The determination of these two additional factors must be archived, in this further investigation.

Received: 5 August 2021; Accepted: 2 September 2021

Published online: 21 September 2021

References

1. Slimene, M. B. & Arbi Khelifi, M. Modelling and study of energy storage devices for photovoltaic lighting. *Energy Explor. Exploit.* **38**, 1932–1945 (2020).
2. Cano, J. M., Martin, A. D., Herrera, R. S., Vazquez, J. R. & Ruiz-Rodriguez, F. J. Grid-connected PV systems controlled by sliding via wireless communication. *Energies* **14**, 1931 (2021).
3. Arifin, A. M., Redzuan, F. M., Kadir, E. A., Ismail, N. & Zain, M. M. Design and sizing water pumping system powered by photovoltaic. *AIP Conf. Proc.* **2306**, 020022 (2020).
4. Luu, M. T., Milani, D., Nomvar, M. & Abbas, A. Dynamic modelling and analysis of a novel latent heat battery in tankless domestic solar water heating. *Energy Build.* **152**, 227–242 (2017).
5. Koçar, G., Eryaşar, A., Gödekmerdan, E., Özgül, S. & Düzenli, M. A Prospect on Integration of Solar Technology to Modern Greenhouses. *Dokuz Eylül Üniversitesi Mühendislik Fakültesi Fen ve Mühendislik Dergisi* **20**, 245–258 (2018).

6. Petrollese, M. & Cocco, D. Techno-economic assessment of hybrid CSP-biogas power plants. *Renew. Energy* **155**, 420–431 (2020).
7. Dincer, I. & Rosen, M. *Thermal Energy Storage: Systems and Applications* (Wiley, 2002).
8. Zhou, D. The acceptance of solar water pump technology among rural farmers of northern Pakistan: A structural equation model. *Cogent Food Agric.* **3**, 1280882 (2017).
9. Aliyu, M. *et al.* A review of solar-powered water pumping systems. *Renew. Sustain. Energy Rev.* **87**, 61–76 (2018).
10. Jenkins, T. Designing solar water pumping systems for livestock NM State University, Cooperative Extension Service, Engineering New Mexico Resource Network, College of Agricultural, Consumer and Environmental Sciences, College of Engineering, 1–12 (2014).
11. Garg, H. P. *Solar Powered Water Pump Advances in Solar Energy Technology* (Springer, 1987).
12. Kumar, P. & Sharma, M. Analysis of heat transfer fluids in concentrated solar power (CSP). *Int. J. Eng. Res. Technol. (IJERT)* **3**, 239–240 (2014).
13. Minea, A. A. & El-Maghlany, W. M. Influence of hybrid nanofluids on the performance of parabolic trough collectors in solar thermal systems: Recent findings and numerical comparison. *Renew. Energy* **120**, 350–364 (2018).
14. Coccia, G., Di Nicola, G., Colla, L., Fedele, L. & Scattolini, M. Adoption of nanofluids in low-enthalpy parabolic trough solar collectors: Numerical simulation of the yearly yield. *Energy Convers. Manag.* **118**, 306–319 (2016).
15. Mwesigye, A. & Meyer, J. P. Optimal thermal and thermodynamic performance of a solar parabolic trough receiver with different nanofluids and at different concentration ratios. *Appl. Energy* **193**, 393–413 (2017).
16. Sekhar, T. V. R., Prakash, R., Nandan, G. & Muthuraman, M. Performance enhancement of a renewable thermal energy collector using metallic oxide nanofluids. *Micro Nano Lett.* **13**, 248–251 (2018).
17. Kharat, P. B., Humbe, A. V., Kounsalye, J. S. & Jadhav, K. M. Thermophysical investigations of ultrasonically assisted magnetic nanofluids for heat transfer. *J. Supercond. Nov. Magn.* **32**, 1307–1317 (2019).
18. Rehan, M. A. *et al.* Experimental performance analysis of low concentration ratio solar parabolic trough collectors with nanofluids in winter conditions. *Renew. Energy* **118**, 742–751 (2018).
19. Okonkwo, E. C., Abid, M. & Ratlamwala, T. A. Numerical analysis of heat transfer enhancement in a parabolic trough collector based on geometry modifications and working fluid usage. *J. Solar Energy Eng.* **140**, 051009 (2018).
20. Toghiani, S., Baniyasi, E. & Afshari, E. Thermodynamic analysis and optimization of an integrated Rankine power cycle and nanofluid based parabolic trough solar collector. *Energy Convers. Manag.* **121**, 93–104 (2016).
21. Benabderrahmane, A., Benazza, A., Aminallah, M. & Laouedj, S. Heat transfer behaviors in parabolic trough solar collector tube with compound technique. *Int. J. Sci. Res. Eng. Technol. (IJSRET)* **5**, 568–575 (2016).
22. Mwesigye, A., Yilmaz, I. H. & Meyer, J. P. Numerical analysis of the thermal and thermodynamic performance of a parabolic trough solar collector using SWCNTs-Therminol[®] VP-1 nanofluid. *Renew. Energy* **119**, 844–862 (2018).
23. Kasaeian, A., Daviran, S., Azarian, R. D. & Rashidi, A. Performance evaluation and nanofluid using capability study of a solar parabolic trough collector. *Energy Convers. Manag.* **89**, 368–375 (2015).
24. Ahmadi, M. H., Mirlohi, A., Nazari, M. A. & Ghasempour, R. A review of thermal conductivity of various nanofluids. *J. Mol. Liq.* **265**, 181–188 (2018).
25. Bellos, E. & Tzivanidis, C. Thermal analysis of parabolic trough collector operating with mono and hybrid nanofluids. *Sustain. Energy Technol. Assess.* **26**, 105–115 (2018).
26. Ekcicler, R., Arslan, K., Turgut, O. & Kurşun, B. Effect of hybrid nanofluid on heat transfer performance of parabolic trough solar collector receiver. *J. Therm. Anal. Calorim.* **143**, 1637–1654 (2021).
27. Sciacovelli, A., Verda, V. & Sciubba, E. Entropy generation analysis as a design tool—A review. *Renew. Sustain. Energy Rev.* **43**, 1167–1181 (2015).
28. Al-Kouz, W. *et al.* Entropy generation optimization for rarified nanofluid flows in a square cavity with two fins at the hot wall. *Entropy* **21**, 103 (2019).
29. Afridi, M. I., Alkanhal, T. A., Qasim, M. & Tlili, I. Entropy generation in Cu–Al₂O₃–H₂O hybrid nanofluid flow over a curved surface with thermal dissipation. *Entropy* **21**, 941 (2019).
30. Khan, M. I., Hafeez, M. U., Hayat, T., Khan, M. I. & Alsaedi, A. Magneto rotating flow of hybrid nanofluid with entropy generation. *Comput. Meth. Prog. Biomed.* **183**, 105093 (2020).
31. Shah, Z., Sheikholeslami, M., Kumam, P. & Shafee, A. Modeling of entropy optimization for hybrid nanofluid MHD flow through a porous annulus involving variation of Bejan number. *Sci. Rep.* **10**, 1–14 (2020).
32. Aziz, A., Jamshed, W., Ali, Y. & Shams, M. Heat transfer and entropy analysis of Maxwell hybrid nanofluid including effects of inclined magnetic field, Joule heating and thermal radiation. *Discrete Contin. Dyn. Syst. S* **13**, 2667 (2020).
33. Jamshed, W. & Aziz, A. Cattaneo–Christov based study of TiO₂–CuO/EG Casson hybrid nanofluid flow over a stretching surface with entropy generation. *Appl. Nanosci.* **8**, 685–698 (2018).
34. Aziz, A., Jamshed, W., Aziz, T., Bahaidarah, H. M. & Rehman, K. U. Entropy analysis of Powell–Eyring hybrid nanofluid including effect of linear thermal radiation and viscous dissipation. *J. Therm. Anal. Calorim.* **143**, 1331–1343 (2021).
35. Sindhu, S. & Gireesha, B. J. Entropy generation analysis of hybrid nanofluid in a microchannel with slip flow convective boundary and non-linear heat flux. *Int. J. Numer. Meth. Heat Fluid Flow* **31**, 53–74 (2020).
36. Das, S., Sarkar, S. & Jana, R. N. Feature of entropy generation in Cu–Al₂O₃/ethylene glycol hybrid nanofluid flow through a rotating channel. *BioNanoSci.* **10**, 950–967 (2020).
37. Alsabery, A. I. *et al.* Entropy generation and natural convection flow of hybrid nanofluids in a partially divided wavy cavity including solid blocks. *Energies* **13**, 2942 (2020).
38. Hussain, A., Malik, M. Y., Awais, M., Salahuddin, T. & Bilal, S. Computational and physical aspects of MHD Prandtl–Eyring fluid flow analysis over a stretching sheet. *Neural Comput. Appl.* **31**, 425–433 (2019).
39. Abbas, N., Malik, M. Y., Alqarni, M. S. & Nadeem, S. Study of three dimensional stagnation point flow of hybrid nanofluid over an isotropic slip surface. *Physica A* **554**, 124020 (2020).
40. Khan, M., Salahuddin, T., Malik, M. Y., Alqarni, M. S. & Alqahtani, A. M. Numerical modeling and analysis of bioconvection on MHD flow due to an upper paraboloid surface of revolution. *Physica A* **553**, 124231 (2020).
41. Abdelmalek, Z., Hussain, A., Bilal, S., Sherif, E. S. M. & Thounthong, P. Brownian motion and thermophoretic diffusion influence on thermophysical aspects of electrically conducting viscoelastic nanofluid flow over a stretched surface. *J. Mater. Res. Technol.* **9**, 11948–11957 (2021).
42. Abbasi, A., Mabood, F., Farooq, W. & Khan, S. U. Radiation and Joule heating effects on electroosmosis-modulated peristaltic flow of Prandtl nanofluid via tapered channel. *Int. Commun. Heat Mass Transf.* **123**, 105183 (2021).
43. Li, Y. M. *et al.* An assessment of the mathematical model for estimating of entropy optimized viscous fluid flow towards a rotating cone surface. *Sci. Rep.* **11**, 10259 (2021).
44. Imran, M., Farooq, U., Muhammad, T., Khan, S. U. & Waqas, H. Bioconvection transport of Carreau nanofluid with magnetic dipole and non-linear thermal radiation. *Case Stud. Therm. Eng.* **26**, 101129 (2021).
45. Khan, M. I., Khan, S. A., Hayat, T., Khan, M. I. & Alsaedi, A. Nanomaterial based flow of Prandtl–Eyring (non-Newtonian) fluid using Brownian and thermophoretic diffusion with entropy generation. *Comput. Meth. Prog. Biomed.* **180**, 105017 (2019).
46. Aziz, A., Jamshed, W. & Aziz, T. Mathematical model for thermal and entropy analysis of thermal solar collectors by using Maxwell nanofluids with slip conditions, thermal radiation and variable thermal conductivity. *Open Phys.* **16**, 123–136 (2018).

47. Reddy, N. B., Poornima, T. & Sreenivasulu, P. Influence of variable thermal conductivity on MHD boundary layer slip flow of ethylene-glycol based Cu nanofluids over a stretching sheet with convective boundary condition. *Int. J. Eng. Math.* **2014**, 905158 (2014).
48. Maxwell, J. C. *A Treatise on Electricity and Magnetism* (Clarendon Press, 1873).
49. Ali, H. M. *Hybrid Nanofluids for Convection Heat Transfer* (Academic Press, 2020).
50. Mukhtar, T., Jamshed, W., Aziz, A. & Kouz, W. A. Computational investigation of heat transfer in a flow subjected to MHD of Maxwell nanofluid over a stretched flat sheet with thermal radiation. *Numer. Methods Partial Differ. Equ.* <https://doi.org/10.1002/num.22643> (2020).
51. Iqbal, Z., Azhar, E. & Maraj, E. N. Performance of nano-powders SiO₂ and SiC in the flow of engine oil over a rotating disk influenced by thermal jump conditions. *Physica A* **565**, 125570 (2021).
52. Brewster, M. Q. *Thermal Radiative Transfer and Features* (Wiley, 1992).
53. Keller, H. B. A new difference scheme for parabolic problems. in *Numerical Solution of Partial Differential Equations-II*, 327–350 (Academic Press, 1971).
54. Ishak, A., Nazar, R. & Pop, I. Mixed convection on the stagnation point flow towards a vertical, continuously stretching sheet. *ASME J. Heat Transf.* **129**, 1087–1090 (2007).
55. Ishak, A., Nazar, R. & Pop, I. Boundary layer flow and heat transfer over an unsteady stretching vertical surface. *Meccanica* **44**, 369–375 (2009).
56. Abolbashari, M. H., Freidoonimehr, N., Nazari, F. & Rashidi, M. M. Entropy analysis for an unsteady MHD flow past a stretching permeable surface in nano-fluid. *Powder Technol.* **267**, 256–267 (2014).
57. Das, S., Chakraborty, S., Jana, R. N. & Makinde, O. D. Entropy analysis of unsteady magneto-nanofluid flow past accelerating stretching sheet with convective boundary condition. *Appl. Math. Mech.* **36**, 1593–1610 (2015).
58. Jamshed, W., Devi, S. U. & Nisar, K. S. Single phase based study of Ag–Cu/EO Williamson hybrid nanofluid flow over a stretching surface with shape factor. *Phys. Scr.* **96**, 065202 (2021).
59. Jamshed, W., Nisar, K. S., Ibrahim, R. W., Shahzad, F. & Eid, M. R. Thermal expansion optimization in solar aircraft using tangent hyperbolic hybrid nanofluid: A solar thermal application. *J. Mater. Res. Technol.* **14**, 985–1006 (2021).
60. Jamshed, W. *et al.* A numerical frame work of magnetically driven Powell–Eyring nanofluid using single phase model. *Sci. Rep.* **11**, 16500 (2021).
61. Jamshed, W. Thermal augmentation in solar aircraft using tangent hyperbolic hybrid nanofluid: A solar energy application. *Energy Environ.* <https://doi.org/10.1177/0958305X211036671> (2021).
62. Jamshed, W. Numerical investigation of MHD impact on Maxwell nanofluid. *Int. Commun. Heat Mass Transf.* **120**, 104973 (2021).
63. Jamshed, W. & Nisar, K. S. Computational single phase comparative study of Williamson nanofluid in parabolic trough solar collector via Keller box method. *Int J. Energy Res.* <https://doi.org/10.1002/er.6554> (2021).
64. Jamshed, W. *et al.* Thermal examination of renewable solar energy in parabolic trough solar collector utilizing Maxwell nanofluid: A noble case study. *Case Stud. Therm. Eng.* **27**, 101258 (2021).
65. Jamshed, W. *et al.* Features of entropy optimization on viscous second grade nanofluid streamed with thermal radiation: a Tiwari and Das model. *Case Stud. Therm. Eng.* **27**, 101291 (2021).
66. Jamshed, W., Akgül, E. K. & Nisar, K. S. Keller box study for inclined magnetically driven Casson nanofluid over a stretching sheet: Single phase model. *Phys. Scr.* **96**, 065201 (2021).
67. Turkyilmazoglu, M. Velocity slip and entropy generation phenomena in thermal transport through metallic porous channel. *J. Non-Equilib. Thermodyn.* **45**, 247–256 (2020).

Acknowledgements

The authors express their appreciation to the Dean ship of Scientific Research at King Khalid University for funding this work through research groups program under grant number R.G.P.2/61/40.

Author contributions

W.J. formulated the problem. W.J., N.A.A.M.N., S.S.P.M.I. and M.R.E., solved the problem. W.J., N.A.A.M.N., S.S.P.M.I., R.S., K.S.N., F.S., M.R.E., A.H.A.A. and I.S.Y. computed and scrutinized the results. All the authors equally contributed to the writing and proofreading of the paper. All authors reviewed the manuscript.

Competing interests

The authors declare no competing interests.

Additional information

Correspondence and requests for materials should be addressed to W.J.

Reprints and permissions information is available at www.nature.com/reprints.

Publisher's note Springer Nature remains neutral with regard to jurisdictional claims in published maps and institutional affiliations.



Open Access This article is licensed under a Creative Commons Attribution 4.0 International License, which permits use, sharing, adaptation, distribution and reproduction in any medium or format, as long as you give appropriate credit to the original author(s) and the source, provide a link to the Creative Commons licence, and indicate if changes were made. The images or other third party material in this article are included in the article's Creative Commons licence, unless indicated otherwise in a credit line to the material. If material is not included in the article's Creative Commons licence and your intended use is not permitted by statutory regulation or exceeds the permitted use, you will need to obtain permission directly from the copyright holder. To view a copy of this licence, visit <http://creativecommons.org/licenses/by/4.0/>.

© The Author(s) 2021